

THE AFTERGLOW AND EARLY-TYPE HOST GALAXY OF THE SHORT GRB 150101B AT $z = 0.1343$

W. FONG^{1,15}, R. MARGUTTI^{2,3}, R. CHORNOCK⁴, E. BERGER⁵, B. J. SHAPPEE^{6,16}, A. J. LEVAN⁷, N. R. TANVIR⁸, N. SMITH¹,
 P. A. MILNE¹, T. LASKAR^{9,10}, D. B. FOX¹¹, R. LUNNAN¹², P. K. BLANCHARD⁵, J. HJORTH¹³, K. WIERSEMA⁸,
 A. J. VAN DER HORST¹⁴, AND D. ZARITSKY¹

¹ Steward Observatory, University of Arizona, 933 N. Cherry Avenue, Tucson, AZ 85721, USA

² Center for Cosmology and Particle Physics, New York University, 4 Washington Place, New York, NY 10003, USA

³ Northwestern University, Department of Physics and Astronomy, 2145 Sheridan Road, Evanston, IL 60208, USA

⁴ Astrophysical Institute, Department of Physics and Astronomy, 251B Clipping Lab, Ohio University, Athens, OH 45701, USA

⁵ Harvard-Smithsonian Center for Astrophysics, 60 Garden Street, Cambridge, MA 02138, USA

⁶ Carnegie Observatories, 813 Santa Barbara Street, Pasadena, CA 91101, USA

⁷ Department of Physics, University of Warwick, Gibbet Hill Road, Coventry CV4 7AL, UK

⁸ Department of Physics & Astronomy, University of Leicester, University Road, Leicester LE1 7RH, UK

⁹ National Radio Astronomy Observatory, 520 Edgemont Road, Charlottesville, VA 22903, USA

¹⁰ Department of Astronomy, University of California, 501 Campbell Hall, Berkeley, CA 94720-3411, USA

¹¹ Department of Astronomy and Astrophysics, Pennsylvania State University, 525 Davey Laboratory, University Park, PA 16802, USA

¹² Department of Astronomy, California Institute of Technology, 1200 East California Boulevard, Pasadena, CA 91125, USA

¹³ Dark Cosmology Centre, Niels Bohr Institute, University of Copenhagen, Juliane Maries Vej 30, DK-2100 Copenhagen, Denmark

¹⁴ Department of Physics, 725 21st Street NW, The George Washington University, Washington, DC 20052, USA

Received 2016 August 30; revised 2016 October 20; accepted 2016 October 22; published 2016 December 14

ABSTRACT

We present the discovery of the X-ray and optical afterglows of the short-duration GRB 150101B, pinpointing the event to an early-type host galaxy at $z = 0.1343 \pm 0.0030$. This makes GRB 150101B the most nearby short gamma-ray burst (GRB) with an early-type host galaxy discovered to date. Fitting the spectral energy distribution of the host galaxy results in an inferred stellar mass of $\approx 7 \times 10^{10} M_{\odot}$, stellar population age of $\approx 2\text{--}2.5$ Gyr, and star formation rate of $\lesssim 0.4 M_{\odot} \text{ yr}^{-1}$. The host of GRB 150101B is one of the largest and most luminous short GRB host galaxies, with a *B*-band luminosity of $\approx 4.3L^*$ and half-light radius of ≈ 8 kpc. GRB 150101B is located at a projected distance of 7.35 ± 0.07 kpc from its host center and lies on a faint region of its host rest-frame optical light. Its location, combined with the lack of associated supernova, is consistent with an NS–NS/NS–BH merger progenitor. From modeling the evolution of the broadband afterglow, we calculate isotropic-equivalent gamma-ray and kinetic energies of $\approx 1.3 \times 10^{49}$ erg and $\approx (6\text{--}14) \times 10^{51}$ erg, respectively, a circumburst density of $\approx (0.8\text{--}4) \times 10^{-5} \text{ cm}^{-3}$, and a jet opening angle of $\gtrsim 9^{\circ}$. Using observations extending to ≈ 30 days, we place upper limits of $\lesssim (2\text{--}4) \times 10^{41} \text{ erg s}^{-1}$ on associated kilonova emission. We compare searches following previous short GRBs to existing kilonova models and demonstrate the difficulty of performing effective kilonova searches from cosmological short GRBs using current ground-based facilities. We show that at the Advanced LIGO/VIRGO horizon distance of 200 Mpc, searches reaching depths of $\approx 23\text{--}24$ AB mag are necessary to probe a meaningful range of kilonova models.

Key words: gamma-ray burst: individual (150101B)

1. INTRODUCTION

The afterglows and host galaxies of short-duration gamma-ray bursts (GRBs; $T_{90} \lesssim 2$ s; Kouveliotou et al. 1993) provide critical information about their explosion properties and progenitors. Modeling of their afterglows from the radio to X-ray bands has led to a median isotropic-equivalent energy scale of $\approx 10^{51}$ erg and low explosion environment densities of $\approx 10^{-3}\text{--}10^{-2} \text{ cm}^{-3}$ (Berger 2007, 2014; Nakar 2007; Nicuesa Guelbenzu et al. 2012; Fong et al. 2015). These properties are in stark contrast to long-duration GRBs ($T_{90} \gtrsim 2$ s), which have a median isotropic-equivalent energy scale of $\approx 10^{53}$ erg (e.g., Nysewander et al. 2009; Laskar et al. 2014) and substantially higher circumburst densities of $\approx 0.1\text{--}100 \text{ cm}^{-3}$ (Panaitescu & Kumar 2002; Yost et al. 2003). Furthermore, the association of long GRBs with Type Ic supernovae (SNe Ic; e.g., Hjorth & Bloom 2012, p. 169) and their exclusive association with star-forming galaxies (Djorgovski et al. 1998; Le Floch et al. 2003;

Fruchter et al. 2006; Wainwright et al. 2007) has helped to establish their origin from massive stars.

In comparison, short GRBs lack associated SNe (Fox et al. 2005; Hjorth et al. 2005a, 2005b; Soderberg et al. 2006; Kocevski et al. 2010; Berger 2014), strongly suggestive of an older stellar progenitor. Furthermore, the detection of an *r*-process kilonova associated with the short GRB 130603B was the first direct evidence linking them to neutron star–neutron star and/or neutron star–black hole merger progenitors (NS–NS/NS–BH; Berger et al. 2013a; Tanvir et al. 2013). The spatial distribution of short GRBs within their hosts, together with their weak correlation with local star formation and stellar mass (Berger 2010; Fong et al. 2010; Fong & Berger 2013; Tunnicliffe et al. 2014), is also fully consistent with expectations for NS–NS/NS–BH mergers (Bloom et al. 1999; Fryer et al. 1999; Belczynski et al. 2006; Zemp et al. 2009; Behroozi et al. 2014).

Critical to the study of short GRB progenitors are their host galaxy properties and demographics. While early studies based on a small sample of events found a dominance of early-type host galaxies (Zheng & Ramirez-Ruiz 2007), a later study

¹⁵ Einstein Fellow.

¹⁶ Hubble Fellow.

focused on 36 short GRBs found that $\approx 20\%$ – 40% of events are hosted by early-type host galaxies, with a dominance of star-forming hosts (Fong et al. 2013). However, the star-forming hosts of short GRBs have lower specific star formation rates (SFRs), higher luminosities, and higher metallicities than the star-forming hosts of long GRBs (Berger 2009). Short GRBs have been discovered over the redshift range $z \approx 0.12$ – 1.3 (see Berger 2014), with the single outlier GRB 090426A at $z = 2.609$ (Antonelli et al. 2009; Levesque et al. 2010). Only two short GRBs¹⁷ have been discovered at $z \lesssim 0.2$: GRB 050709 ($z = 0.161$) and GRB 080905A ($z = 0.1218$), both of which have star-forming host galaxies (Fox et al. 2005; Hjorth et al. 2005b; Rowlinson et al. 2010). A third event, GRB 061201, is potentially associated with a star-forming galaxy at $z = 0.111$; however, this association is less robust (Stratta et al. 2007; Fong et al. 2010). In general, events at low redshift offer an opportunity to study their explosion and host galaxy environments in great detail.

Here, we report the discovery of the optical and X-ray afterglows of the short GRB 150101B, which localizes the event to an early-type host galaxy at $z = 0.1343 \pm 0.003$ ($D = 636.7$ Mpc). This makes GRB 150101B the most nearby short GRB discovered in an early-type host galaxy to date. An earlier work concentrated on broadband modeling of the host galaxy to uncover an active galactic nucleus (AGN) at the host center (Xie et al. 2016). Here, we seek to provide a comprehensive view of this event. In Section 2, we present the discovery of the optical and X-ray afterglows, as well as optical and near-IR host galaxy observations. In Section 3, we analyze the broadband afterglow to infer the burst explosion properties, and place deep limits on SN and kilonova emission. In Section 4, we determine the host galaxy redshift, stellar population and morphological properties, and the location of GRB 150101B within its host. In Section 5, we compare the properties of GRB 150101B and its host to previous short GRBs. In particular, we discuss the implications for the progenitors and for future kilonova searches. We draw conclusions in Section 6.

Unless otherwise noted, all magnitudes in this paper are in the AB system and are corrected for Galactic extinction in the direction of the burst using $E(B - V) = 0.036$ mag and $R_V = 3.1$ (Schlegel et al. 1998; Schlafly & Finkbeiner 2011). Reported uncertainties correspond to 68% confidence, unless otherwise indicated. We employ a standard Λ CDM cosmology with $\Omega_M = 0.286$, $\Omega_\Lambda = 0.714$, and $H_0 = 69.6$ km s⁻¹ Mpc⁻¹.

2. OBSERVATIONS OF GRB 150101B

GRB 150101B was detected on 2015 January 1 at 15:23 UT (Cummings 2015) by the Burst Alert Telescope (BAT; Barthelmy et al. 2005) on board the *Swift* satellite and by the Gamma-ray Burst Monitor (GBM) on board the *Fermi* satellite at 15:23:35 UT (Cummings 2015). *Swift*/BAT localized the burst to R.A. = $12^{\text{h}}32^{\text{m}}10^{\text{s}}.4$ and decl. = $-10^{\circ}58'48''$ (J2000) with $2'.4$ -radius precision (90% containment; Lien et al. 2016). The 15–150 keV γ -ray emission consists of a single pulse with a duration of $T_{90} = 0.012 \pm 0.009$ s (Lien et al. 2016), classifying GRB 150101B as a short-duration GRB with no extended emission. Employing a power-law fit for the BAT

spectrum gives a fluence of $f_\gamma = (6.1 \pm 2.2) \times 10^{-8}$ erg cm⁻² and a photon index of $\Gamma_\gamma = 1.4 \pm 0.6$ in the 15–150 keV energy band ($\chi^2_\nu = 0.7$; 90% confidence; Lien et al. 2016). The fluence measured by *Fermi*/GBM, which covers a wider energy range than *Swift* of 10–1000 keV, is $f_\gamma = (1.09 \pm 0.14) \times 10^{-7}$ erg cm⁻². The spectrum is best fit by a power law with index $\Gamma_\gamma = 1.70 \pm 0.09$ (Stanbro 2015), consistent with the value measured from the *Swift*/BAT data.

2.1. Afterglow Observations and Discovery

2.1.1. Optical Afterglow Discovery

We obtained *r*-band observations of GRB 150101B with the Inamori Magellan Areal Camera and Spectrograph (IMACS) mounted on the Magellan/Baade 6.5 m telescope at a mid-time of 2015 January 03.297 UT ($\delta t = 1.66$ days, where δt is the time after the BAT trigger in the observer frame). The observations cover the entire BAT position (Figure 1 and Table 1). To assess variability of any optical sources within the BAT position, we obtained a second set of IMACS observations at $\delta t \approx 2.65$ days. Performing digital image subtraction between the two sets of observations using the ISIS software package (Alard 2000), we find a faint point-like residual $\approx 3''$ southeast of a bright galaxy (Figure 1), indicative of a fading optical source.

To assess the nature of this source and its association with GRB 150101B, we obtained two deeper sets of *r*-band observations with the Gemini Multi-Object Spectrograph (GMOS) mounted on the Gemini-South 8 m telescope at a mid-time of $\delta t \approx 10.70$ days and with Magellan/IMACS at $\delta t \approx 48.39$ days (Table 1). We perform digital image subtraction between each of the initial epochs and the last set of Magellan observations at $\delta t \approx 48.39$ days, which serves as the deepest template. In the first two subtractions, a point-like residual source is present at the same position, which we consider to be the optical afterglow of GRB 150101B (Figure 1).

To determine the position of the optical afterglow, we perform absolute astrometry between the earliest Magellan observations and the Two Micron All Sky Survey (2MASS) catalog using the IRAF astrometry routines `ccmap` and `ccsetwcs`. Using 19 common point sources, the resulting 1σ astrometric tie uncertainty is $\sigma_{2\text{MASS} \rightarrow \text{GRB}} = 0''.24$. Since the position of the afterglow is contaminated by galaxy light in our discovery images, we use `SEXTRACTOR`¹⁸ to determine the afterglow position and uncertainty (σ_{GRB}) in the subtracted images. The subtraction between the first and last epochs ($\delta t = 1.66$ and 48.39 days, respectively) yields a positional uncertainty of $\sigma_{\text{GRB}} = 0''.029$. We therefore calculate an absolute optical afterglow position of R.A. = $12^{\text{h}}32^{\text{m}}05^{\text{s}}.094$, decl. = $-10^{\circ}56'03''00$ (J2000), with a total 1σ positional uncertainty of $0''.24$.

To measure the brightness of the afterglow in our first two Magellan observations, we perform point-spread function (PSF) photometry using standard PSF-fitting routines in the IRAF/`daophot` package. We note that the position of the afterglow is contaminated either by flux from the nearby galaxy in the observations or by residuals from the saturated galaxy core in the subtracted images (Figure 1), preventing accurate aperture photometry. We create a model PSF using three to five

¹⁷ The long-duration GRBs 060505 and 060614 are associated with star-forming galaxies at $z = 0.0894$ and $z = 0.125$, respectively. These events lack associated SNe to deep limits, suggesting that they do not have massive star progenitors (Gal-Yam et al. 2006; Ofek et al. 2007).

¹⁸ <http://www.astromatic.net/software/sextractor>

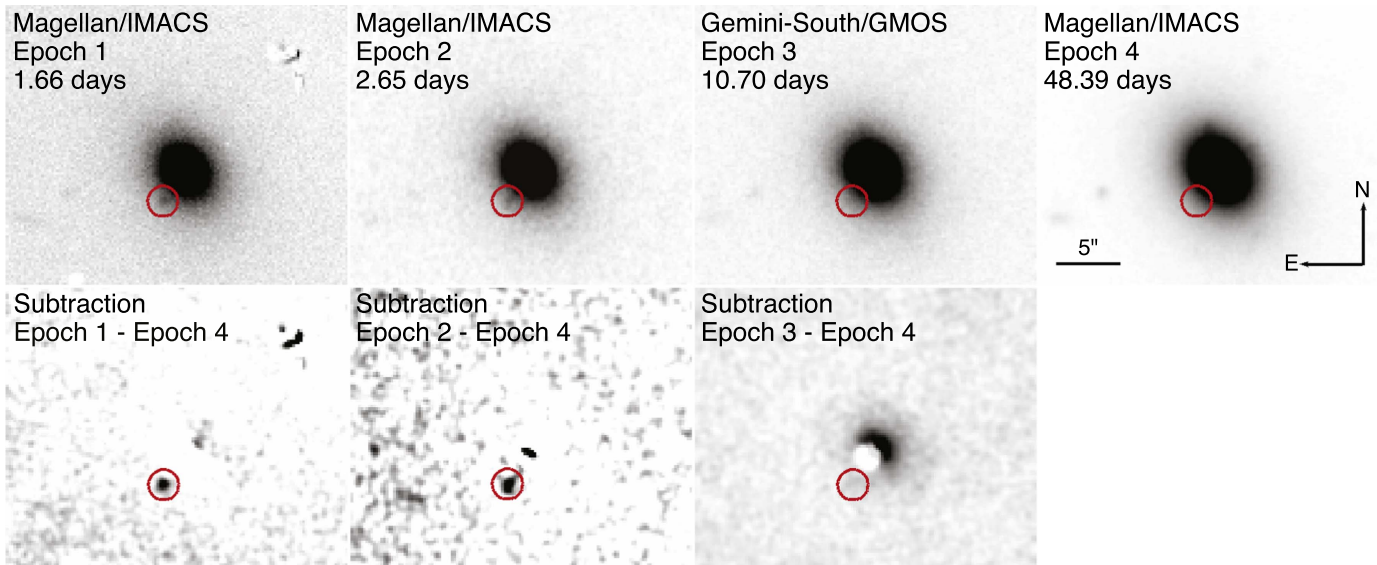


Figure 1. Optical r -band observations of the afterglow of GRB 150101B. Imaging was obtained with IMACS mounted on the Magellan/Baade 6.5 m telescope and GMOS mounted on the Gemini-South 8 m telescope at four separate epochs, $\delta t = 1.66, 2.65, 10.70,$ and 48.39 days (observer frame). Digital image subtractions between the last epoch and each of the previous epochs reveal a fading optical afterglow at R.A. = $12^{\text{h}} 32^{\text{m}} 05^{\text{s}}.094$ and decl. = $-10^{\circ} 56' 03''.00$ (J2000), with a 1σ positional uncertainty of $0''.24$ (red circle; 5σ radius). Due to saturation of the host galaxy core and differences in seeing between the epochs, the position of the afterglow in the subtractions is contaminated by residuals from the host galaxy subtraction, necessitating PSF photometry to properly measure the afterglow brightness. Image subtractions have been smoothed with a 2 pixel Gaussian, and the scale and orientation of all panels are as shown in the fourth panel.

bright, unsaturated stars in each field out to a radius of $4.5\theta_{\text{FWHM}}$ from the center of each star, and then use this PSF to subtract 20 additional stars in this field. The clean subtraction of these stars indicates an accurate model of the PSF for the observation. We then use the model PSF to subtract a point source fixed at the location of the afterglow. We calibrate all of the photometry relative to the Gemini observations at $\delta t = 10.70$ days, which were taken in photometric conditions, using the most recent tabulated zero point. Taking into account the uncertainty in the zero point, as well as the Galactic extinction in the direction of the burst (Schlafly & Finkbeiner 2011), we measure an afterglow brightness of $r_{\text{AB}} = 23.01 \pm 0.17$ mag and $r_{\text{AB}} = 23.53 \pm 0.26$ mag at $\delta t = 1.66$ and 2.65 days, respectively. Our optical observations and afterglow photometry, supplemented by published values from the literature, are summarized in Table 1.

To obtain upper limits on any transient optical flux from our late-time Gemini and Magellan observations, we inject fake sources of varying brightness into each observation at the position of the optical afterglow using IRAF/addstar. We then perform PSF photometry and measure the uncertainty for each of the fake sources to determine the 3σ upper limit on the afterglow in each image. The resulting limits are listed in Table 1.

2.1.2. Near-IR Upper Limits

We obtained several observations of GRB 150101B with the High Acuity Wide field K-band Imager I (HAWK-I) mounted on the Very Large Telescope (VLT) in Chile in the $YJHK$ filters, spanning $\delta t \approx 2.66$ – 43.63 days (Table 1). We used standard routines as part of the `esorex` pipeline for dark subtraction, flat-field correction, and stacking. For the series of $YJHK$ observations on 2015 January 4, guiding issues during these observations resulted in an elongated PSF with a bright core, making the comparison with subsequent observations challenging, as well as reducing the resulting depth, with

varying impact on each filter. In Table 1, we give point-source limits from small-aperture photometry. We obtained photometric calibration via 2MASS, although Y -band observations were calibrated against tabulated zero points and confirmed by a comparison of USNO-B1 I -band and 2MASS J -band observations of common sources. The elongated PSF means that the reported limits are shallower than might be expected. We obtained additional H -band observations on 2015 January 16 and February 14. These provide deep limits on the presence of any transient emission, reaching $H_{\text{AB}} \gtrsim 23.4$. The details of our observations, as well as 3σ limits, are listed in Table 1.

2.1.3. X-Ray Afterglow Discovery

Observations with the X-ray Telescope (XRT; Burrows et al. 2005) on board *Swift* commenced at $\delta t = 139.2$ ks and revealed an X-ray source with a UVOT-enhanced position of R. A. = $12^{\text{h}} 32^{\text{m}} 04^{\text{s}}.96$ and decl. = $-10^{\circ} 56' 00''.7$ (J2000) and an uncertainty of $1''.8$ in radius (90% containment; Evans et al. 2007, 2009; Cummings et al. 2015). However, this X-ray source was found to remain constant in flux over the duration of the XRT observations, $\delta t \approx 139.2$ – 2612 ks. Furthermore, the position of this X-ray source is coincident with the nucleus of the host galaxy (see Section 2.2), which is a known galaxy 2MASX J12320498-1056010 as cataloged in the NASA/IPAC Extragalactic Database (Helou et al. 1991, pp. 89–106). No other fading source from the *Swift*/XRT observations was reported.

We analyze X-ray observations obtained at a mid-time of 2015 January 9.565 UT ($\delta t \approx 7.94$ days) with the Advanced CCD Imaging Spectrometer (ACIS-S) on board the *Chandra* X-ray Observatory (ID: 16508492; PI: E. Troja), with a net exposure time of 14.9 ks. We retrieve the preprocessed Level 2 data from the *Chandra* archive and use the CIAO/`wavdetect` routine to perform a blind search of X-ray sources at or near the optical afterglow position. We find an X-ray source located at R.A. = $12^{\text{h}} 32^{\text{m}} 05^{\text{s}}.099$ and decl. = $-10^{\circ} 56' 02''.80$,

Table 1
GRB 150101B Optical and Near-IR Afterglow and Host Galaxy Observations

Date (UT)	δt (days)	Telescope	Instrument	Band	Exposures (s)	Afterglow (AB mag)	$F_{\nu, \text{opt}}$ (μJy)	Host (AB mag)	A_{λ} (AB mag)
2015 Jan 3.297	1.66	Magellan/Baade	IMACS	<i>r</i>	8×150	23.01 ± 0.17	2.27 ± 0.36	...	0.094
2015 Jan 4.289	2.65	Magellan/Baade	IMACS	<i>r</i>	10×120	23.53 ± 0.26	1.41 ± 0.34	...	0.094
2015 Jan 4.298	2.66	VLT	HAWK-I	<i>J</i>	12×60	>22.3	<4.37	...	0.029
2015 Jan 4.310	2.67	VLT	HAWK-I	<i>H</i>	12×60	>21.4	<10.0	...	0.018
2015 Jan 4.322	2.68	VLT	HAWK-I	<i>K</i>	12×60	>21.5	<9.12	...	0.012
2015 Jan 4.359	2.72	VLT	HAWK-I	<i>Y</i>	22×60	>20.5	<22.9	...	0.043
2015 Jan 11.261	9.62	TNG ^a	NICS	<i>J</i>	...	>21.7	<7.59	...	0.029
2015 Jan 12.341	10.70	Gemini-South	GMOS	<i>r</i>	19×90	>24.2	<0.76	...	0.094
2015 Jan 16.201	14.56	TNG ^a	NICS	<i>J</i>	...	>22.4	<3.98	...	0.029
2015 Jan 16.307	14.67	VLT	HAWK-I	<i>H</i>	22×60	>23.4	<1.58	...	0.018
2015 Jan 16.331	14.69	VLT	HAWK-I	<i>Y</i>	22×60	>23.6	<1.32	...	0.043
2015 Jan 21.533	19.89	UKIRT	WFCAM	<i>J</i>	12×200	>22.4	<3.98	15.47 ± 0.05	0.029
2015 Jan 21.569	19.93	UKIRT	WFCAM	<i>K</i>	12×200	>22.2	<4.79	15.11 ± 0.05	0.012
2015 Jan 30.508	28.87	UKIRT	WFCAM	<i>J</i>	12×200	>23.0	<2.29	15.55 ± 0.05	0.029
2015 Jan 30.544	28.90	UKIRT	WFCAM	<i>K</i>	12×200	>22.4	<3.98	15.20 ± 0.06	0.012
2015 Feb 11.320	40.70	<i>HST</i>	WFC3/IR	F160W	3×250	>25.3	<0.28	15.09 ± 0.01	0.021
2015 Feb 11.385	40.74	<i>HST</i>	WFC3/UVIS	F606W	4×350	>25.1	<0.33	16.57 ± 0.01	0.102
2015 Feb 14.274	43.63	VLT	HAWK-I	<i>H</i>	22×60	>23.9	<1.00	...	0.018
2015 Feb 19.036	48.39	Magellan/Baade	IMACS	<i>r</i>	8×150	>24.6	<0.52	...	0.094
2015 Feb 19.048	48.41	Magellan/Baade	IMACS	<i>r</i>	3×45	16.51 ± 0.04	0.094
2015 Feb 19.053	48.41	Magellan/Baade	IMACS	<i>g</i>	3×60	17.42 ± 0.04	0.136
2015 Feb 19.058	48.42	Magellan/Baade	IMACS	<i>i</i>	3×45	16.08 ± 0.04	0.070
2015 Feb 19.063	48.42	Magellan/Baade	IMACS	<i>z</i>	3×60	15.77 ± 0.05	0.052

Note. All upper limits correspond to 3σ confidence, and uncertainties correspond to 1σ confidence. All values are corrected for Galactic extinction in the direction of the burst, A_{λ} (Schlafly & Finkbeiner 2011).

^a From D’Avanzo et al. (2015).

Table 2
GRB 150101B *Chandra* Afterglow Observations

δt (days)	Exposure Time (s)	$F_{\text{X}}(0.3\text{--}10\text{ keV})^{\text{a}}$ ($\text{erg cm}^{-2}\text{ s}^{-1}$)	$F_{\nu}(1\text{ keV})$ (μJy)	Γ_{X}	$N_{\text{H, int}}$ (cm^{-2})
7.94	14869	$(1.16 \pm 0.12) \times 10^{-13}$	$(1.08 \pm 0.11) \times 10^{-2}$	1.67 ± 0.17	$\lesssim 3.0 \times 10^{21}$
39.68	14862	$(2.08 \pm 0.50) \times 10^{-14}$	$(1.94 \pm 0.47) \times 10^{-3}$	1.13 ± 0.49	$\lesssim 2.1 \times 10^{21}$

Note. Uncertainties correspond to 1σ , and upper limits correspond to 3σ confidence.

^a Unabsorbed flux.

with a 1σ positional uncertainty of $0''.38$, coincident with the position of the optical afterglow (Section 2.1). Within a $1''.2$ -radius aperture, we compute a net count rate of 9.5×10^{-3} counts s^{-1} (0.5–8 keV), which corresponds to a significance of $\sim 52\sigma$.

To assess the variability of this X-ray source, we analyze a second set of *Chandra*/ACIS-S observations obtained at a mid-time of 2015 February 10.305 UT ($\delta t \approx 39.68$ days; ID: 16708496, PI: A. Levan). Fixing the position and aperture to those derived from the first *Chandra* epoch, we compute a net count rate of 1.3×10^{-3} counts s^{-1} (0.5–8 keV), which corresponds to a significance of $\sim 6\sigma$. This indicates that the source has faded by a factor of ≈ 7 between $\delta t \approx 7.94$ and 39.68 days. Due to the fading of this source, as well as the spatial coincidence with the optical afterglow, we confirm this source as the X-ray afterglow of GRB 150101B. We note that the X-ray afterglow position and count rates are fully consistent with an independent analysis of the *Chandra* data by Xie et al. (2016).

To determine the flux calibration, we extract a spectrum from each of the *Chandra* epochs using CIAO/specextract.

We fit each of the data sets with an absorbed power-law model with photon index, Γ_{X} , and intrinsic neutral hydrogen absorption column, $N_{\text{H, int}}$, in excess of the Galactic column density in the direction of the burst, $N_{\text{H, MW}} = 3.48 \times 10^{20}\text{ cm}^{-2}$; (typical uncertainty of $\sim 10\%$; Kalberla et al. 2005; Wakker et al. 2011), using Cash statistics. For the first epoch, we find a best-fitting spectrum characterized by $\Gamma_{\text{X}} = 1.67 \pm 0.17$ and a 3σ upper limit of $N_{\text{H, int}} \lesssim 3.0 \times 10^{21}\text{ cm}^{-2}$ (C-stat $_{\nu} = 0.85$ for 92 dof). For the second epoch, the best-fitting spectrum is characterized by $\Gamma_{\text{X}} = 1.13 \pm 0.49$ and $N_{\text{H, int}} \lesssim 2.1 \times 10^{21}\text{ cm}^{-2}$ (C-stat $_{\nu} = 1.21$ for 13 dof). We use the spectral parameters to calculate the count-rate-to-flux conversion factors, and hence the unabsorbed fluxes, in the 0.3–10 keV energy band. The details of the *Chandra* observations, 0.3–10 keV fluxes, and best-fit spectral parameters are listed in Table 2. To enable comparison of the X-ray light curves to the optical and radio data, we also convert the X-ray fluxes to flux densities, $F_{\nu, \text{X}}$, at a fiducial energy of 1 keV ($F_{\nu, \text{X}} \propto \nu^{\beta_{\text{X}}}$ where $\beta_{\text{X}} \equiv 1 - \Gamma_{\text{X}}$); these values are listed in Table 2.

2.1.4. Radio Upper Limit

We observed the position of GRB 150101B with the Karl G. Jansky Very Large Array (VLA; Program 14A-344, PI: E. Berger) beginning at $\delta t \approx 5.73$ days at a mean frequency of 9.8 GHz (upper and lower sidebands centered at 8.6 and 11.0 GHz, respectively) using 3C 286 bandpass/flux calibration and J1239-1023 for gain calibration. We utilize the Astronomical Image Processing System (AIPS; Greisen 2003, p. 109) for data calibration and analysis. The positions of the X-ray and optical afterglows are contaminated by radio emission from the host galaxy (see Section 2.2). To place a limit on any radio emission at the location of the afterglow, we use AIPS/IMSTAT with the position fixed to that of the optical afterglow and calculate the average flux within a region fixed to the size of the radio beam. In this manner, we calculate a 3σ upper limit of $\lesssim 1.5$ mJy for the radio afterglow of GRB 150101B.

2.2. Host Galaxy Observations

2.2.1. Optical Imaging and Identification

The optical afterglow of GRB 150101B is situated $\approx 3''$ southeast of galaxy 2MASX J12320498-1056010 as cataloged in the NASA/IPAC Extragalactic Database (Helou et al. 1991, pp. 89–106). We obtained a set of late-time observations with Magellan/IMACS at a mid-time of $\delta t \approx 48.4$ days in the *griz*-bands (Table 1 and Figure 1). To measure the absolute position of the galaxy, we use the IRAF routines `xregister` and `wscopy` to align the late-time observations with the afterglow discovery image, which is tied to 2MASS. This gives an absolute position of R.A. = $12^{\text{h}} 32^{\text{m}} 04.^{\text{s}} 973$ and decl. = $-10^{\circ} 56' 00''.50$ (J2000), with a total 1σ positional uncertainty of $0''.24$, where the dominant source of uncertainty is the astrometric tie error. Taking into account the afterglow and host positional uncertainties, we calculate a relative offset between the location of the afterglow and galaxy center of δR . A. = $-1''.89$ and $\delta\text{decl.} = 2''.50$, for a total angular offset of $\delta R = 3.07 \pm 0''.03$.

We use IRAF/`apphot` to perform aperture photometry of the galaxy, where the zero point is calibrated to a standard-star field taken on the same night at similar airmass. We use a $9''$ -radius source aperture for all bands, where the aperture size is chosen to encompass the entire galaxy and maximize the signal-to-noise ratio. We utilize source-free regions surrounding the galaxy as background regions. The optical and near-IR photometry is listed in Table 1. We note that the photometric errors are dominated by uncertainties in the zero points.

Given the angular separation, δR , and the optical galaxy brightness of $r_{\text{AB}} = 16.51 \pm 0.04$ mag, we calculate a probability of chance coincidence (see Bloom et al. 2002; Berger 2010) of $P_{\text{cc}} \approx 4.8 \times 10^{-4}$. The low probability of chance coincidence, combined with the lack of any galaxies in the field with similarly low values, makes 2MASX J12320498-1056010 the definitive host galaxy of GRB 150101B.

2.2.2. Near-IR

We obtained two sets of near-IR observations in the *JK* bands with the Wide-field Camera (WFCAM; Casali et al. 2007) mounted on the 4 m United Kingdom Infrared Telescope (UKIRT) starting at $\delta t \approx 19.89$ and 28.87 days, respectively (Table 1). We obtained preprocessed images from

the WFCAM Science Archive (Hamly et al. 2008) that are corrected for bias, flat field, and dark current by the Cambridge Astronomical Survey Unit.¹⁹ For each epoch and filter, we co-add the images and perform astrometry relative to 2MASS using a combination of tasks in Starlink²⁰ and IRAF. To assess the presence of transient near-IR emission, we perform digital image subtraction between the two sets of observations in each filter and find no evidence for variability. Calibrated to 2MASS, we calculate 3σ limits of $J_{\text{AB}} \gtrsim 22.4$ mag and $K_{\text{AB}} \gtrsim 22.2$ mag at $\delta t \approx 19.9$ days (Table 1). Also listed are limits from near-IR observations published in the literature. We perform host galaxy photometry in the same manner as in the optical band (Section 2.2.1) and measure $J_{\text{AB}} = 15.47 \pm 0.05$ mag and $K_{\text{AB}} = 15.11 \pm 0.05$ mag (Table 1).

2.2.3. HST Observations

We retrieved preprocessed images from the *Hubble Space Telescope* (HST) archive²¹ taken with the Wide Field Camera 3 (WFC3) at $\delta t \approx 40.7$ days (PI: N. Tanvir) in two filters, F606W and F160W, which utilize the UV and IR channels of WFC3, respectively. We apply distortion corrections and combine the individual exposures using the `astrodrizzle` package in PyRAF (Gonzaga 2012). For the WFC3/IR images, we use the recommended values of `pixfrac` = 1.0 and `pixscale` = $0''.13 \text{ pixel}^{-1}$, while for the WFC3/UVIS images, we use `pixscale` = $0''.04 \text{ pixel}^{-1}$. We use standard routines in IRAF to perform aperture photometry of the host galaxy and use PSF photometry to calculate upper limits; the results are listed in Table 1.

We perform relative astrometry between the HST and IMACS afterglow discovery images using IRAF astrometry routines. Taking into account the positional uncertainties of the afterglow and host, as well as the astrometric tie error between the HST and afterglow images, we calculate relative astrometric uncertainties of $\sigma_{\text{F160W}} = 0''.07$ and $\sigma_{\text{F606W}} = 0''.04$.

2.2.4. Spectroscopy

We obtained spectroscopic observations of the host on 2015 January 4.26 UT using Magellan/IMACS at a mean airmass of 2.0. We obtained a pair of 600 s exposures with the 300+17.5 grism covering 3900–10000 Å at a spectral resolution of ~ 3.9 Å. The $0''.7$ slit was aligned at a position angle of 323° to go through both the nucleus of the host galaxy and the GRB position. IMACS has an atmospheric dispersion compensator, so the relative flux scale is reliable. We used standard tasks in IRAF to reduce the spectra and performed wavelength calibration using He–Ne–Ar arc lamps. We used observations of the standard stars LTT 1020 and LTT 3864 (Hamuy et al. 1994) and custom IDL programs to apply a flux calibration and remove the telluric absorption bands. We calibrate the overall flux using the measured F606W, *g*-, *r*-, and *i*-band host photometry (Table 1).

2.2.5. Archival Observations: A Low-luminosity AGN

There are archival observations of the host of GRB 150101B, spanning the far-ultraviolet to the radio bands from GALEX, XMM, 2MASS, WISE, and the VLA. Using these observations,

¹⁹ <http://casu.ast.cam.ac.uk/>

²⁰ <http://starlink.eao.hawaii.edu/starlink>

²¹ <http://archive.stsci.edu/hst/>

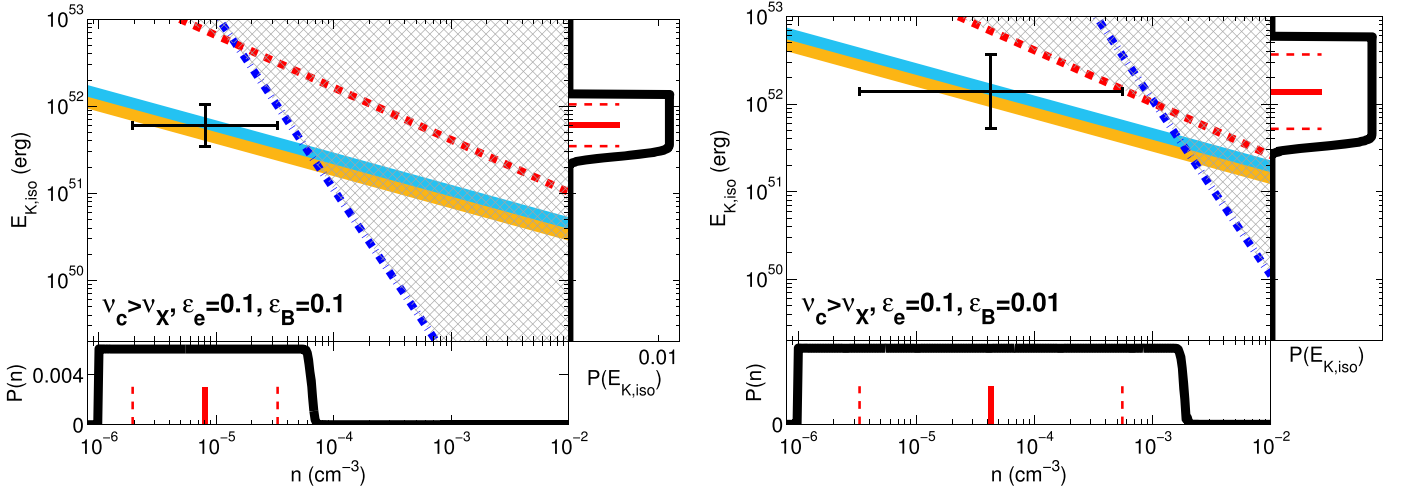


Figure 2. Parameter space of isotropic-equivalent kinetic energy and circumburst density for GRB 150101B. Left: parameter space assuming fiducial values for the microphysical parameters of $\epsilon_e = \epsilon_B = 0.1$, where each of the afterglow measurements provides an independent constraint: X-rays (light blue) and optical (orange). The width of each solid region corresponds to 1σ uncertainty. The upper limits from the radio band (red dashed line) and cooling frequency (dark-blue dot-dashed line) are also shown. The regions of parameter space ruled out by the observations are shown by gray hatched regions. The median solution and 1σ uncertainty are indicated by the black cross in each panel. The joint probability distributions in n , with an imposed lower bound of $n_{\min} = 10^{-6} \text{ cm}^{-3}$ (bottom panel), and $E_{K,iso}$ (right panel) are shown. Red lines correspond to the median in each parameter, and dotted lines correspond to the 1σ uncertainty. Right: same as the left panel, but for values of $\epsilon_e = 0.1$ and $\epsilon_B = 0.01$.

as well as *Chandra* and Westerbork Synthesis Radio Telescope (WSRT) observations taken after the GRB, Xie et al. (2016) found that the broadband spectral energy distribution matches that of a low-luminosity AGN. They classify the host galaxy as an X-ray-bright, optically normal galaxy, with an X-ray luminosity of $\approx 7.5 \times 10^{42} \text{ erg s}^{-1}$ (0.2–10 keV; Xie et al. 2016). We discuss further evidence for AGN activity in the optical spectrum in Section 4.2.

3. AFTERGLOW PROPERTIES

3.1. Energy Scale and Circumburst Density

To constrain the explosion properties and circumburst environment, we compare the radio through X-ray observations of GRB 150101B to the standard synchrotron model. We adopt a constant-density medium model (Sari et al. 1998; Granot & Sari 2002), a reasonable assumption for a nonmassive star progenitor. This model provides a mapping from the broadband afterglow observations to the burst physical properties: the isotropic-equivalent kinetic energy ($E_{K,iso}$), circumburst density (n), fractions of post-shock energy in radiating electrons (ϵ_e) and magnetic fields (ϵ_B), and the electron power-law distribution index (p), with $N(\gamma) \propto \gamma^{-p}$ for $\gamma \gtrsim \gamma_{\min}$, where γ_{\min} is the minimum Lorentz factor of the electron distribution.

To determine the locations of the synchrotron break frequencies with respect to the X-ray, optical, and radio bands and thus constrain the burst explosion properties, we calculate the electron power-law index p , using a combination of temporal and spectral information. The temporal and spectral power-law indices are given by α and β , respectively, where $F_\nu \propto t^{\alpha\nu^\beta}$. To determine α_X and α_{opt} , we utilize χ^2 -minimization to fit a single power-law model to each light curve in the form $F_\nu \propto t^\alpha$. In this manner, we measure $\alpha_X = -1.07 \pm 0.15$ and $\alpha_{\text{opt}} = -1.02^{+0.44}_{-0.55}$ for the X-ray and optical light curves, respectively. Computing α_{opt} and 1σ uncertainties using the detections alone marginally violates the upper limit at $\delta t \approx 10.70$ days; therefore, we use the observation at ≈ 10.70 days to set the upper limit on the decline rate, resulting in

asymmetric uncertainties. The afterglow light curves, along with the best-fit power-law models, are shown in Figures 3 and 6 below. From the X-ray spectral fit, we find $\beta_X \equiv 1 - \Gamma_X = -0.67 \pm 0.17$ (Section 2.1.3 and Table 2).

To determine the location of the cooling frequency, ν_c , to the observing bands, we compare the temporal and spectral indices to the closure relations (Sari et al. 1999; Granot & Sari 2002). If $\nu_c < \nu_X$, then the independently derived values for p from the temporal and spectral indices are inconsistent: $p = 2.1 \pm 0.2$ from α_X , $p = 1.3 \pm 0.3$ from β_X , and $p = 2.0 \pm 0.73$ from α_{opt} . On the other hand, for $\nu_c > \nu_X$, the values are fully consistent: $p = 2.4 \pm 0.2$ from α_X , $p = 2.3 \pm 0.3$ from β_X , and $p = 2.4 \pm 0.7$ from α_{opt} . Furthermore, if $\nu_c > \nu_X$, then $\beta_X = \beta_{\text{OX}}$, where β_{OX} is the optical-to-X-ray spectral index. Indeed, extrapolating the *Chandra* data to the time of the optical afterglow using α_X , we calculate $\beta_{\text{OX}} \approx -0.61$, which is consistent with the value of $\beta_X = -0.67 \pm 0.17$. Therefore, for the rest of our calculations, we utilize a value of $p = 2.40 \pm 0.17$ as determined by the weighted average and assume $\nu_c > \nu_X$. We note that this is also equal to the average value for p inferred from the short GRB population (Fong et al. 2015).

Next, we determine a set of constraints on n and $E_{K,iso}$ based on the X-ray and optical flux densities, the radio upper limit, and the condition that $\nu_c > \nu_X$. Using the X-ray flux density, $z = 0.1343$, luminosity distance $d_L = 1.96 \times 10^{27} \text{ cm}$, $\nu_X = 2.4 \times 10^{17} \text{ Hz}$ (1 keV), $\nu_{\text{opt}} = 4.8 \times 10^{14} \text{ Hz}$ (*r*-band), and $p = 2.4$, we obtain the relation (Granot & Sari 2002)

$$n^{0.5} E_{K,iso,52}^{1.35} \epsilon_{e,-1}^{1.4} \epsilon_{B,-1}^{0.85} \approx (1.6 \pm 0.2) \times 10^{-3} \quad (1)$$

where n is in units of cm^{-3} , $E_{K,iso,52}$ is in units of 10^{52} erg , and $\epsilon_{e,-1}$ and $\epsilon_{B,-1}$ are in units of 0.1. The 1σ uncertainty is dominated by the uncertainty in the individual flux measurements. The constraint on $E_{K,iso} - n$ parameter space from the X-ray afterglow is shown in Figure 2, where the width of the region represents the 1σ uncertainty. We calculate an independent constraint from the optical flux density, assuming

that the optical frequency is between the peak frequency, ν_m , and the cooling frequency, ν_c , such that $\nu_m < \nu_{\text{opt}} < \nu_c$. Thus, the optical and X-ray bands occupy the same spectral regime and have the same dependencies on the physical parameters. We calculate the constraint,

$$n^{0.5} E_{\text{K,iso},52}^{1.35} \epsilon_{e,-1}^{1.4} \epsilon_{B,-1}^{0.85} \approx (8.3 \pm 1.3) \times 10^{-4}, \quad (2)$$

shown in Figure 2. Next, we impose a constraint from the radio band under the assumption that the radio band is between the self-absorption frequency and the peak frequency such that $\nu_a < \nu_{\text{radio}} < \nu_m$. Using the radio upper limit and $\nu_{\text{radio}} = 9.8 \times 10^9$ Hz, we obtain the constraint

$$n^{1/2} E_{\text{K,iso},52}^{5/6} \epsilon_{e,-1}^{-2/3} \epsilon_{B,-1}^{1/3} \gtrsim 1.5 \times 10^{-2}. \quad (3)$$

where the constraint imposed on the $E_{\text{K,iso}} - n$ is shown in Figure 2. Using the fact that $\nu_c > \nu_X$, we can use the relative location of the cooling frequency as a final constraint. Setting the cooling break to a minimum value, $\nu_{c,\text{min}} = 2.4 \times 10^{18}$ Hz (10 keV), at the upper end of the X-ray band, we calculate the relation

$$n^{-1} E_{\text{K,iso},52}^{-1/2} \epsilon_{B,-1}^{-3/2} \gtrsim 3.0 \times 10^4. \quad (4)$$

We use Equations (1)–(4) and joint probability analysis (described in Fong et al. 2015) to solve for the isotropic-equivalent kinetic energy and circumburst density. For $\epsilon_e = \epsilon_B = 0.1$, we calculate $n = 8.0_{-6.1}^{+25.2} \times 10^{-6} \text{ cm}^{-3}$ and $E_{\text{K,iso}} = 6.1_{-2.6}^{+4.5} \times 10^{51}$ erg (Figure 2). For $\epsilon_e = 0.1$ and $\epsilon_B = 0.01$, we find $n = 4.3_{-3.9}^{+51.1} \times 10^{-5} \text{ cm}^{-3}$ and $E_{\text{K,iso}} = 1.4_{-0.9}^{+2.3} \times 10^{52}$ erg (1σ uncertainties). From a comparison of the optical and X-ray afterglow emission, we find no evidence for extinction intrinsic to the burst site or host galaxy (e.g., $A_V^{\text{host}} = 0$). We note that the values for the kinetic energy and density differ slightly from our previous analysis, which included GRB 150101B (Fong et al. 2015) due to a refinement of the optical and X-ray fluxes.

Finally, we calculate the isotropic-equivalent γ -ray energy, by $E_{\gamma,\text{iso}} = 4\pi d_L^2 (1+z)^{-1} f_{\gamma}^{\text{bol}}$ erg. Using the *Swift*/BAT 15–150 keV fluence and a bolometric correction factor of 5 to correspond to a wider γ -ray energy range of ≈ 10 –1000 keV, we calculate $E_{\gamma,\text{iso}} = (1.3 \pm 0.3) \times 10^{49}$ erg.

3.2. Jet Opening Angle

We can use the temporal evolution of the afterglow to constrain the jet opening angle. We have no observations of the X-ray afterglow at $\delta t \lesssim 8$ days and therefore no information on the early decline rate. However, the optical and X-ray bands are on the same spectral slope (Section 3), and their afterglows should exhibit the same temporal decline. Indeed, the optical afterglow at $\delta t \approx 1.7$ –2.7 days has a decline rate of $\alpha_{\text{opt}} \approx -1.02$, matching the X-ray decline rate at $\delta t \approx 7.9$ –39.7 days of $\alpha_X \approx -1.07$ within the 1σ uncertainties. Thus, the combination of the early optical data and the late-time X-ray data implies that the afterglow is on a single power-law decline over $\delta t \approx 1.7$ –39.7 days. Since jet collimation is predicted to produce a temporal “break” in the light curve (“jet break”; Sari et al. 1999), the single power-law decline can be used to place a lower limit on the opening angle assuming on-axis orientation. The late-time X-ray observations, in

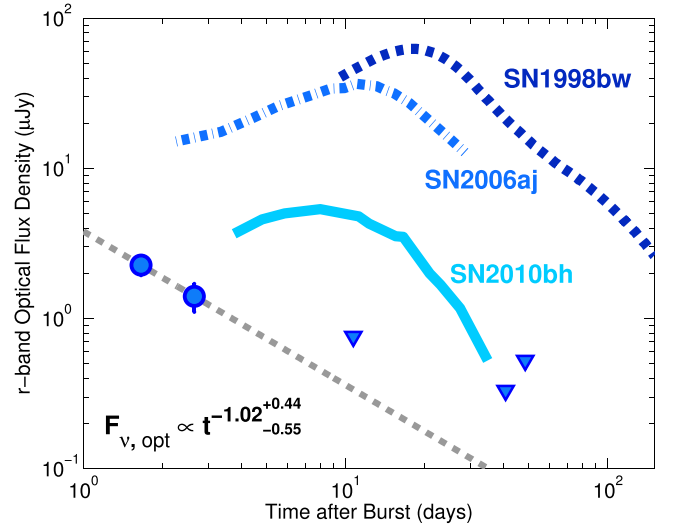


Figure 3. Optical r -band afterglow light curve of GRB 150101B (blue circles and triangles). Error bars correspond to 1σ confidence, and triangles denote 3σ upper limits. The best-fit power-law model (gray dashed line) is characterized by a temporal decay of $\alpha_{\text{opt}} \approx -1.02$. Also shown are the optical light curves of three SNe that represent the range of luminosities observed for GRB-SNe: GRB-SN 1998bw (dark-blue dotted line; Galama et al. 1998; Clocchiatti et al. 2011), GRB-SN 2006aj (blue dot-dashed line; Mirabal et al. 2006), and GRB-SN 2010bh (light-blue line; Olivares et al. 2012); the GRB-SN light curves have all been corrected for extinction and redshifted to $z = 0.1343$. The optical limits are a factor of ≈ 6 –60 below the luminosities of known GRB-SNe, ruling out the presence of an SN associated with GRB 150101B to deep limits.

conjunction with the energy, density, and redshift, can be converted to a jet opening angle, θ_j , using (Sari et al. 1999; Frail et al. 2001)

$$\theta_j = 9.5 t_{j,d}^{3/8} (1+z)^{-3/8} E_{\text{K,iso},52}^{-1/8} n_0^{1/8} \text{ deg}, \quad (5)$$

where $t_{j,d}$ is in days. Using $t_{j,d} > 39.68$ days, which corresponds to the last X-ray observation (Table 2), and using the values for the isotropic-equivalent kinetic energy and circumburst density as determined in Section 3, we calculate a lower limit on the opening angle of $\theta_j \gtrsim 9^\circ$.

3.3. Limits on a Supernova or Kilonova

We utilize our observations at $\delta t \gtrsim 10$ days to place limits on the presence of SN or kilonova emission associated with GRB 150101B. First, we compare our optical r -band observations in the range of $\delta t \approx 10$ –50 days to the light curves of known SNe associated with long-duration GRBs to place limits on SN emission associated with GRB 150101B. We utilize optical light curves of three SNe that represent the range of luminosities observed for GRB-SNe: GRB-SN 1998bw (Galama et al. 1998; Clocchiatti et al. 2011), GRB-SN 2006aj (Mirabal et al. 2006), and GRB-SN 2010bh (Olivares et al. 2012), redshifted to $z = 0.1343$ (Figure 3). At $\delta t \approx 10.7$ days, the limit on the optical flux density from GRB 150101B is $F_{\nu,\text{opt}} \lesssim 0.76 \mu\text{Jy}$, a factor of ≈ 6 –60 below the expected brightness of GRB-SNe (Figure 3). Similarly, the limits at $\delta t \approx 40.7$ and 48.4 days are a factor of ≈ 30 –65 below the expected luminosity of GRB-SN 1998bw (Figure 3). Thus, we can rule out the presence of an SN associated with GRB 150101B to deep limits.

To place limits on emission from a kilonova associated with GRB 150101B, we compare our deep optical and near-IR

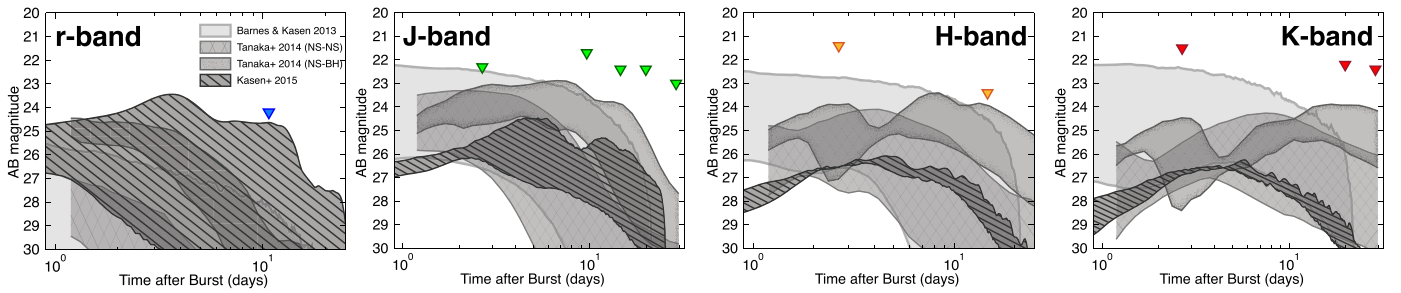


Figure 4. Optical r -band and near-IR JHK -band observations of GRB 150101B in the range of $\delta t \approx 2.6$ –30 days, where triangles denote 3σ upper limits. Also shown are four sets of kilonova models in gray regions: spherically symmetric ejecta from NS–NS mergers (solid; Barnes & Kasen 2013), ejecta from NS–NS mergers (crossed) and NS–BH mergers (speckled; Hotokezaka et al. 2013; Tanaka & Hotokezaka 2013; Tanaka et al. 2014), and outflows from disk winds surrounding a long-lived remnant (single stripes; Kasen et al. 2015). The gray regions represent the full range of light curves considered in each set, assuming pole-on orientation and r -process element opacities.

observations in the range of $\delta t \approx 10.7$ –28.9 days to kilonova models from the literature. We note that the available models truncate at $\delta t > 30$ days. The deepest optical limits during this time range are $r_{\text{AB}} \gtrsim 24.2$ mag at $\delta t \approx 10.7$ days and $Y_{\text{AB}} \gtrsim 23.6$ at $\delta t \approx 14.7$ days. Similarly, the deepest near-IR limits in this time range are $J_{\text{AB}} \gtrsim 23.0$ mag, $H_{\text{AB}} \gtrsim 23.4$ mag, and $K_{\text{AB}} \gtrsim 22.4$ mag (Table 1 and Figure 4).

We consider emission from four sets of kilonova models: (i) spherically symmetric ejecta from NS–NS mergers for a range of ejecta velocities ($0.1c$ – $0.3c$) and ejecta masses (10^{-3} – $10^{-1} M_{\odot}$; Barnes & Kasen 2013), (ii) dynamical ejecta from NS–NS mergers considering “soft” and “stiff” equations of state for the merger components (Hotokezaka et al. 2013; Tanaka & Hotokezaka 2013), (iii) NS–BH mergers considering “soft” and “stiff” equations of state for the neutron star and varying spin for the black hole (Tanaka et al. 2014), and (iv) winds from an accretion disk surrounding a long-lived central compact remnant for remnant lifetimes of 0 ms to ∞ (Kasen et al. 2015). We utilize models that have employed r -process element (as opposed to iron-like) opacities, where model (i) assumes opacities calculated from a few representative lanthanide elements, while models (ii)–(iii) incorporate all of the r -process element opacities. For models (ii)–(iv), we select the pole-on orientation light curves. For each observing band, we use models in the corresponding rest-frame band (e.g., $\lambda_{\text{rest}} = \lambda_{\text{obs}}(1+z)^{-1}$), convert the provided light curves to apparent magnitude, and shift the light curves to the observer frame. The models, along with the late-time optical and near-IR limits, are shown in Figure 4. Although these observations place among the deepest limits on kilonova emission following a short GRB to date (see Section 5.3), they do not constrain the brightest models. This demonstrates the difficulty of placing constraints on kilonovae associated with short GRBs at cosmological redshifts based on the current era of kilonova models.

4. HOST GALAXY PROPERTIES

4.1. Redshift

Since the optical afterglow is faint and rapidly fading, we rely on the host galaxy to determine the redshift of GRB 150101B. Thus, we fit the IMACS spectrum of the host galaxy using simple stellar population (SSP) models at fixed ages of $\tau = 0.64$ –11 Gyr (Bruzual & Charlot 2003). We fit models over the wavelength range 4400–8500 Å as the signal-to-noise ratio is too low to contribute significantly to the

fit at wavelengths outside this range. Using χ^2 -minimization, the resulting best-fit model has a redshift of $z = 0.1343 \pm 0.030$, determined primarily by the location of the main absorption features of $H\beta$, $\text{Mg } b \lambda 5175$ and $\text{NaD} \lambda 5892$ (Figure 5), and a stellar population age of 2.5 Gyr ($\chi^2_{\nu} \approx 5.0$ for 1471 degrees of freedom) assuming solar metallicity. If we allow models to deviate from solar metallicity, adequate fits are also found for stellar population ages of 1.4 and 5 Gyr, while poorer fits are found for SSPs with younger or older ages. Due to the deep absorption features, lack of emission lines, and old inferred stellar population age, we conclude that this host is an early-type galaxy. The spectrum does not require any intrinsic extinction, consistent with the afterglow. We note that this redshift is fully consistent with the reported redshift from the VLT (Levan et al. 2015).

4.2. Stellar Population Properties

While the SSP templates provide adequate matches to several of the main absorption features, a strong $H\alpha$ absorption feature is notably absent (Figure 5). Two possible explanations are emission from the underlying AGN (see Section 2.2.5; Xie et al. 2016) or star formation from a younger stellar population, both of which would cause the $H\alpha$ absorption to be “filled in.”

To assess these contributions, we subtract the 2.5 Gyr template from the host spectrum (Figure 5). We find a clear emission feature at the location of $H\alpha$ with an integrated flux of $F_{\text{H}\alpha} \approx 1.3 \times 10^{-15} \text{ erg s}^{-1} \text{ cm}^{-2}$, or $L_{\text{H}\alpha} \approx 5.5 \times 10^{40} \text{ erg s}^{-1}$ at $z = 0.1343$. To help distinguish between an AGN and star formation, we use archival 1.4 GHz observations as part of the NRAO VLA Sky Survey (Condon et al. 1998), where the host galaxy is detected with $F_{\nu, 1.4 \text{ GHz}} \approx 10.2 \text{ mJy}$. Using standard relations between radio luminosity, $H\alpha$ emission, and star formation (Kennicutt et al. 1994; Yun & Carilli 2002; Murphy et al. 2011), we find that if the radio emission is due to star formation, the expected $H\alpha$ luminosity is ≈ 500 times above the observed value. A large SFR is also in contradiction with the early-type galaxy spectrum and lack of emission lines; thus, star formation is not playing a large role. Instead, the $H\alpha$ emission can naturally be explained by the AGN, as narrow $H\alpha$ emission is common in the optical spectra of a wide variety of AGNs (e.g., Véron-Cetty & Véron 2000). Since $H\alpha$ is contaminated by the AGN, we use the observed $H\alpha$ flux to set an upper limit on the SFR. Using standard relations from Kennicutt et al. (1994), we calculate $\text{SFR} \lesssim 0.4 M_{\odot} \text{ yr}^{-1}$ for the host galaxy of GRB 150101B.

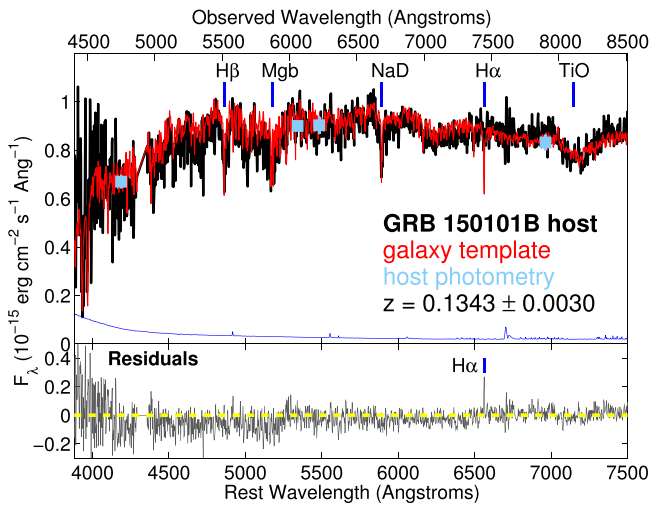


Figure 5. Top: Magellan/Baade IMACS spectrum of the early-type host galaxy of GRB 150101B, binned with a 3-pixel boxcar (black: data; blue: error spectrum), and normalized to the flux of the host galaxy in the *gri* bands and *HST*/F606W as determined from aperture photometry (light blue squares). Also shown is an SSP template (red; Bruzual & Charlot 2003) with a stellar population age of 2.5 Gyr at a redshift of $z = 0.1343 \pm 0.0030$. Fits are performed on the unbinned data, and the chip gap ($\lambda_{\text{rest}} \approx 4293\text{--}4355\text{\AA}$) is excluded from the fit. The locations of the Balmer absorption lines, Mg *b* $\lambda 5175$, NaD $\lambda 5892$, and TiO $\lambda 7050$ are labeled. Bottom: Subtraction of the galaxy template from the GRB 150101B host spectrum, revealing emission at the location of H α $\lambda 6563$, which indicates the presence of an underlying AGN.

We note that we do not detect any continuum emission or spectral features at the position of the afterglow. In particular, the lack of emission lines indicates that there is no ongoing star formation at the location of GRB 150101B.

To determine the stellar mass and stellar population age, we use the Fitting and Assessment of Synthetic Templates (FAST; Kriek et al. 2009) code to fit the host galaxy optical and near-IR photometry to a stellar population synthesis template. We fix the redshift to $z = 0.1343$ and assume solar metallicity, allowing the extinction, stellar population age, and stellar mass to vary. We include all available host photometry in the fit: *grizJK* bands from ground-based telescopes and F606W/F160W from *HST* (Table 1). We find a best-fit template characterized by a stellar population age of $\tau = 2.0_{-0.7}^{+0.8}$ Gyr and stellar mass of $M_{\star} = 7.1_{-2.3}^{+1.2} \times 10^{10} M_{\odot}$ (1σ uncertainties; $\chi^2_{\nu} = 1.5$). Our results are independent of the choice of template library or initial mass function within the 1σ uncertainties. We find poorer fits when assuming subsolar or supersolar metallicities. We note that the age derived from the host galaxy photometry is in good agreement with the results from spectroscopic fitting.

We utilize the host spectrum to calculate the expected *B*-band magnitude as none of the observing bands correspond to rest-frame *B* band. We calculate the average spectral flux over 100\AA centered at $\lambda_{\text{rest}} = 4450\text{\AA}$ and find $F_{\lambda} \approx 7.6 \times 10^{-16} \text{ erg cm}^{-2} \text{ s}^{-1} \text{\AA}^{-1}$; this value does not significantly change for assumed widths of $10\text{--}500\text{\AA}$. The apparent rest-frame *B*-band magnitude is therefore ≈ 17.2 AB mag, corresponding to an absolute magnitude of $M_B = -21.7$, or $L_B \approx 6.9 \times 10^{10} L_{\odot}$. From a comparison to the local *B*-band luminosity function, which gives $M_B^* = -20.2$ (Ilbert et al. 2005), we infer $L_B \approx 4.3 L^*$ for the host of GRB 150101B.

4.3. Morphological Properties

To determine the shape and size of the host galaxy, we use the IRAF/*ellipse* routine to generate elliptical intensity isophotes and construct one-dimensional radial surface brightness profiles. We utilize the late-time *HST* observations as these provide the highest angular resolution. For each observation, we allow the center, ellipticity, and position angle of each isophote to vary.

Using a χ^2 -minimization grid search, we fit each profile with a Sérsic model with index n ($n=1$ is equivalent to an exponential disk profile, and $n=4$ is the de Vaucouleurs profile typical of elliptical galaxies), effective radius r_e , and surface brightness μ_e . In our grid search, n , r_e , and μ_e are the three free parameters. A single Sérsic component provides an adequate fit ($\chi^2_{\nu} \approx 1.0$) in both filters. The best-fit models are characterized by $n = 5.0 \pm 0.1$ and $r_e = 9.5 \pm 0.3$ kpc in the optical F606W filter and $n = 4.1 \pm 0.1$ and $r_e = 7.2 \pm 0.2$ kpc in the F160W near-IR filter. Both fits demonstrate an elliptical morphology.

4.4. Location

We determine the location of GRB 150101B with respect to its host galaxy center and light distribution. The angular offset is $\delta R = 3.07 \pm 0''.03$ (Section 2.2.1), which translates to a projected physical offset of 7.35 ± 0.07 kpc at $z = 0.1343$. Using the effective radius of the host galaxy measured in the F606W and F160W filters, the host-normalized offsets are $0.8r_e$ and $1.0r_e$ in the optical and near-IR bands, respectively.

To determine the brightness of the galaxy at the burst location with respect to the host light distribution, we calculate the fraction of total light in pixels fainter than the afterglow position (“fractional flux”; Fruchter et al. 2006). Since this relies on high angular resolution, we use the *HST* observations, where the 1σ uncertainties on the afterglow positions are $\sigma_{\text{F160W}} = 0''.07$ and $\sigma_{\text{F606W}} = 0''.04$ as determined by relative astrometry (Section 2.2.3). We calculate the average flux among the pixels spanned by the afterglow and create an intensity histogram of a region centered on the host galaxy. We consider pixels with a 1σ brightness level above the Gaussian sky brightness distribution to be part of the host galaxy light (e.g., corresponding to a signal-to-noise ratio of 1). We then plot the pixel flux distribution and determine the fraction of light in pixels fainter than the afterglow pixel. In this manner, we calculate fractional flux values of 0.21 (F606W) and 0.34 (F160W).

5. DISCUSSION

5.1. Afterglow and Explosion Properties

We compare the inferred afterglow and burst explosion properties of GRB 150101B to previous events. With an observed duration of $T_{90} \approx 0.012$ s, GRB 150101B has one of the shortest durations for an event detected by *Swift* or *Fermi* to date (Lien et al. 2016). This holds true when comparing its intrinsic, rest-frame duration of ≈ 0.011 s to the population of *Swift*-detected short GRBs with determined redshifts (Lien et al. 2016). The temporal evolution of the X-ray and optical afterglows is characterized by power-law decline rates that are consistent with the median values for the short GRB population of $\langle \alpha_X \rangle \approx -1.07$ and $\langle \alpha_{\text{opt}} \rangle \approx -1.07$ (Fong et al. 2015). The detection of the X-ray afterglow of GRB 150101B extends to

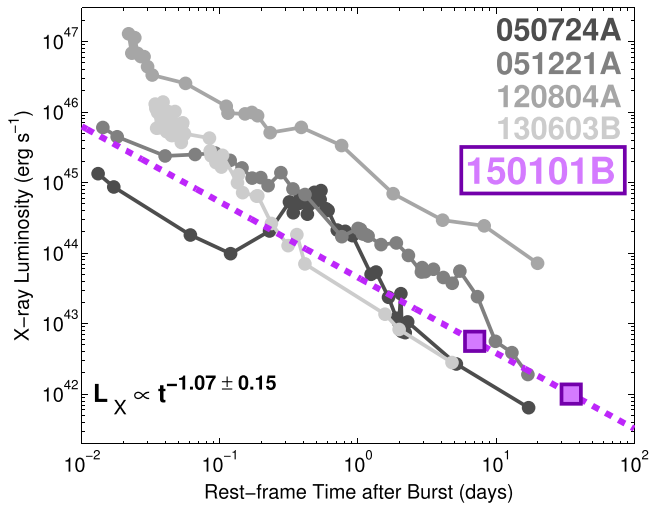


Figure 6. X-ray afterglow light curve of GRB 150101B in the rest frame of the burst (purple squares). The best-fit power-law model (purple dashed line) is characterized by a temporal decay of $\alpha_X = -1.07 \pm 0.15$. Also shown are the X-ray light curves of four short GRBs with late-time X-ray observations and determined redshifts (gray circles): GRB 050724A (Grupe et al. 2006), GRB 051221A (Burrows et al. 2006; Soderberg et al. 2006), GRB 120804A (Berger et al. 2013b), and GRB 130603B (Fong et al. 2014). The light curves are truncated at $\delta t \lesssim 0.01$ day for clarity, and gray lines connect observations for the same burst. The low redshift of GRB 150101B, coupled with the moderate decline rate of $L_X \propto t^{-1.07}$ at late times, allows for the detection of the X-ray afterglow to an unprecedented time of $\delta t_{\text{rest}} \approx 35$ days.

$\delta t \approx 40$ days, corresponding to a rest-frame time of $\delta t_{\text{rest}} \approx 35$ days.

To put GRB 150101B in the context of other events, we collect X-ray light curves for all *Swift* short GRBs that have multiple detections beyond $\delta t_{\text{rest}} \gtrsim 1$ day and determined redshifts. These selection criteria result in four events: GRB 050724A (Grupe et al. 2006), GRB 051221A (Burrows et al. 2006; Soderberg et al. 2006), GRB 120804A (Berger et al. 2013b), and GRB 130603B (Fong et al. 2014). For GRB 150101B and each of the previous events, we convert the X-ray flux (0.3–10 keV) to luminosity and shift the light curve to the rest frame of the burst. The resulting X-ray light curves are shown in Figure 6. GRB 150101B has an X-ray luminosity of $L_X \approx 5.6 \times 10^{42}$ erg s $^{-1}$ at $\delta t_{\text{rest}} \approx 7.0$ days, similar to the X-ray luminosities of previous short GRBs at the same epoch (Figure 6). Previously, short GRBs have only been detected to $\delta t_{\text{rest}} \approx 20$ days. The low redshift of GRB 150101B, coupled with the moderate decline rate of $L_X \propto t^{-1.07}$ at late times, allows for the detection of the X-ray afterglow to an unprecedented time of $\delta t_{\text{rest}} \approx 35$ days.

We compare our inferred values of the explosion properties for GRB 150101B to those for the population of *Swift* short GRBs. We calculate median values for the isotropic-equivalent energies of $E_{\gamma, \text{iso}} \approx 1.3 \times 10^{49}$ erg and $E_{K, \text{iso}} \approx (6\text{--}14) \times 10^{51}$ erg, where the range is due to uncertainty in the microphysical parameters. From the combination of the X-ray and optical afterglows, we infer a lower limit on the jet opening angle of $\theta_j \gtrsim 9^\circ$ for GRB 150101B. Using 9° as the minimum opening angle, we find minimum beaming-corrected energies of $E_\gamma \gtrsim 1.6 \times 10^{47}$ erg and $E_K \gtrsim (7.4\text{--}17) \times 10^{49}$ erg. Compared to *Swift* short GRBs, the isotropic-equivalent γ -ray energy of GRB 150101B is one of the lowest values for short GRBs, while the inferred isotropic-equivalent kinetic energy is at the 60%–70% level of the population (Fong et al. 2015). Assuming a constant-density medium, we also infer an

extremely low median circumburst density of $\approx (0.8\text{--}4.3) \times 10^{-5}$ cm $^{-3}$ (for $\epsilon_B = 0.01\text{--}0.1$), which is in the bottom $\approx 1/4$ of all events, and at the median level when compared to short GRBs that originated in elliptical host galaxies (Fong et al. 2015). These low densities are commensurate with predictions for NS–NS mergers (Montes et al. 2016), as population synthesis for mergers in large, $10^{11} M_\odot$ galaxies predicts that a significant fraction of systems should occur in environments with gas densities of $\lesssim 10^{-3}$ cm $^{-3}$ (Belczynski et al. 2006).

5.2. Host Galaxy Environment: Implications for the Progenitor

At $z = 0.1343$, GRB 150101B is the closest short GRB with an early-type host galaxy to date. The host association is extremely robust, with a probability of chance coincidence of $P_{\text{cc}} \approx 5 \times 10^{-4}$. A single more nearby event,²² GRB 080905A, likely occurred in a star-forming host galaxy at $z = 0.1218$, with $P_{\text{cc}} \approx 0.01$ (Rowlinson et al. 2010). Overall, short GRBs in early-type galaxies comprise $\approx 30\%$ of the population and are detected to $z \sim 1$ (Fong et al. 2013), similar to the host galaxy demographics of SNe Ia (e.g., Sullivan et al. 2006). Both populations are indicative of older stellar progenitors. In contrast, long GRBs exclusively occur in star-forming galaxies (Wainwright et al. 2007; Savaglio et al. 2009), consistent with their massive star progenitors. Furthermore, the lack of associated SNe demonstrates that GRB 150101B did not form from a massive star progenitor.

From fitting of the optical to near-IR SED, we infer stellar population properties for the host: a stellar mass of $\approx 7 \times 10^{10} M_\odot$ ($\log(M_*/M_\odot) \approx 10.9$), stellar population age of $\approx 2\text{--}2.5$ Gyr (at solar metallicity), SFR of $\lesssim 0.4 M_\odot \text{ yr}^{-1}$, and B-band luminosity of $\approx 6.9 \times 10^{10} L_\odot$ ($\approx 4.3L^*$; Table 3). These properties are consistent within 2σ with the values inferred from an independent analysis of the radio to X-ray SED (Xie et al. 2016). The stellar mass and stellar population age are well matched to the eight previous short GRBs with early-type host galaxies, which have stellar masses of $\log(M_*/M_\odot) \approx 9.7\text{--}11.8$ and stellar population ages of $\approx 0.8\text{--}4.4$ Gyr (Table 3). The host of GRB 150101B is one of the most luminous early-type host galaxies, surpassed only by GRB 050509B with $5.0L^*$ (Bloom et al. 2006). This is commensurate with its large relative size of ≈ 8 kpc. Overall, the global host galaxy properties indicate an evolved stellar population and are consistent with those expected for an older stellar progenitor. Notably, this is the first evidence for an AGN in a GRB host galaxy; the paucity of GRB-AGN systems is perhaps not surprising given the rates of low-luminosity AGNs and well-studied GRB hosts (Xie et al. 2016).

Another important diagnostic to evaluate the progenitor is the location of GRB 150101B with respect to its host galaxy. Indeed, a hallmark signature of NS–NS/NS–BH mergers are natal kicks imparted to the compact objects during their formation (e.g., Fryer et al. 1998; Fryer 2004). Coupled with the ~ 1 Gyr delay times, this results in a population of events with a range of separations from their hosts (Perma & Belczynski 2002; Belczynski et al. 2006; Behroozi et al. 2014). We calculate a kick velocity for GRB 150101B by assuming that the progenitor system formed with the most recent stellar population

²² The short GRB 061201 has a possible association with a star-forming host galaxy at $z = 0.111$, but with a relatively high $P_{\text{cc}} \approx 0.1\text{--}0.2$ (Stratta et al. 2007; Fong et al. 2010).

Table 3
Short GRB Early-type Host Galaxy Properties

GRB	z	P_{cc}	$\log(M_*)$ (M_\odot)	Age (Gyr)	L_B (L)	SFR ($M_\odot \text{ yr}^{-1}$)	References
050724A	0.257	2×10^{-5}	10.8	0.94	1.0	$\lesssim 0.05$	1–3
050509B	0.225	5×10^{-3}	11.6	3.18	5.0	$\lesssim 0.15$	3, 4–5
060502B	0.287	0.03	11.8	1.3	1.6	0.8	3, 6
070809	0.473	0.03	11.4	3.07	1.9	$\lesssim 0.1$	3, 7
070729	0.8	0.05	10.6	0.98	1.0	$\lesssim 1.5$	3
090515	0.403	0.15	11.2	4.35	1.0	0.1	3, 7–8
100117A	0.915	7×10^{-5}	10.3	0.79	0.5	$\lesssim 0.2$	3, 9
100625A	0.452	0.04	9.7	0.8	0.2	$\lesssim 0.3$	10
150101B	0.1343	5×10^{-4}	10.9	2–2.5	4.3	$\lesssim 0.4$	This work

Note. The columns are as follows: (1) GRB name, (2) host galaxy redshift, (3) probability of chance coincidence, (4) stellar mass, (5) stellar population age as determined from fitting to single stellar population models, (6) rest-frame B -band luminosity, (7) star formation rate.

References. (1) Berger et al. 2005; (2) Berger 2009; (3) Leibler & Berger 2010; (4) Gehrels et al. 2005; (5) Bloom et al. 2006; (6) Bloom et al. 2007; (7) Berger 2010; (8) Berger 2014; (9) Fong et al. 2011; (10) Fong et al. 2013.

of ≈ 2 –2.5 Gyr. Using the projected physical offset of ≈ 7.4 kpc, this implies a minimum kick velocity of $v_{\min} \approx 2.9 \text{ km s}^{-1}$ for the progenitor of GRB 150101B. However, a more reasonable value for the kick velocity takes into account the host velocity dispersion (v_{disp}), such that $v_{\text{kick}} \approx \sqrt{v_{\min} v_{\text{disp}}}$. Assuming $v_{\text{disp}} \approx 250 \text{ km s}^{-1}$ as determined from $\approx 10^{11} M_\odot$ elliptical galaxies (Forbes & Ponman 1999), we find $v_{\text{kick}} \approx 27$ –30 km s^{-1} for GRB 150101B. This is on the low end of the inferred natal kick velocities for the eight known Galactic NS–NS binaries, which range from ≈ 5 to 500 km s^{-1} (Fryer & Kalogera 1997; Willems et al. 2004; Wong et al. 2010). We note that Xie et al. (2016) inferred an older stellar population age of $\approx 5.7 \pm 1.0$ Gyr, which would translate to a lower kick velocity of $v_{\text{kick}} \approx 16$ –20 km s^{-1} . The fractional flux value of $\approx 20\%$ –35% demonstrates that GRB 150101B occurred on a faint region of its host rest-frame optical light and is thus weakly correlated with local stellar mass. Furthermore, there is no evidence for ongoing star formation at the position of GRB 150101B. These findings are also commensurate with NS/BH kicks.

We note that magnetars have also been suggested as viable progenitors of short GRBs. In particular, the accretion-induced collapse (AIC) of a WD or WD–WD merger product may lead to the delayed formation of a magnetar, subsequently producing a flare that would be seen as a short GRB (Levan et al. 2006; Metzger et al. 2008; Bucciantini et al. 2012). Such events are predicted to trace stellar mass and thus occur primarily in early-type galaxies (Levan et al. 2006). However, unlike NS–NS/NS–BH mergers, these systems would not experience significant kicks. GRB 150101B is weakly correlated with its local stellar mass, making NS/BH kicks a more viable option for this event. Furthermore, the low predicted rates of such AIC events make them unlikely to contribute significantly to the short GRB rate (Dessart et al. 2007).

5.3. Constraints on Kilonova Emission

A predicted signal of NS–NS/NS–BH mergers is transient emission from the radioactive decay of heavy elements produced in the merger ejecta (r -process “kilonova”; Li & Paczyński 1998; Kulkarni 2005; Metzger et al. 2010). The signal is predicted to be dominant in the near-IR bands due to the heavy-element opacities (Barnes & Kasen 2013; Rosswog et al. 2013; Tanaka & Hotokezaka 2013), although models

incorporating a long-lived NS remnant predict bluer colors (Metzger & Fernández 2014; Kasen et al. 2015). A near-IR excess detected with *HST* observations following the short GRB 130603B was interpreted as kilonova emission and the first direct evidence that short GRBs originate from NS–NS/NS–BH mergers (Berger et al. 2013a; Tanvir et al. 2013).

For GRB 150101B, we place limits of $\approx (2\text{--}4) \times 10^{41} \text{ erg s}^{-1}$ on kilonova emission (Figure 7). To compare these limits to searches for late-time emission following previous short GRBs, we collect all available data from the short GRB afterglow catalog (Fong et al. 2015), constraining the sample to bursts with upper limits at $\delta t_{\text{rest}} \gtrsim 0.1$ days to match the timescale of kilonova light curves. We only include events that have either rest-frame r - or J -band observations. For 15 bursts with no determined redshift, we assume the median of the short GRB population, $z = 0.5$, to convert to luminosity. In addition to GRB 150101B, 25 short GRBs have rest-frame optical limits, and seven events have rest-frame near-IR limits. These limits, along with the GRB 130603B kilonova detection (Berger et al. 2013a; Tanvir et al. 2013) and four sets of kilonova models (described in Section 3.3), are displayed in Figure 7. We note that since GRB 061201 has a relatively uncertain association with a galaxy at $z = 0.111$, we also display the limit if this burst originated at the median redshift of $z = 0.5$ (Figure 7).

In the rest-frame optical band, GRB 150101B has one of the deepest limits on optical kilonova emission to date with $\approx 2 \times 10^{41} \text{ erg s}^{-1}$, and the most stringent for a short GRB with a secure redshift. For GRB 061201, if the true redshift is $z = 0.111$, this event has the deepest limit of $\approx 6 \times 10^{40} \text{ erg s}^{-1}$. This limit can rule out the optically brightest models that invoke an *indefinitely* stable NS remnant (Kasen et al. 2015), while an assumption of a higher-redshift origin at $z = 0.5$ is not stringent enough to place any meaningful constraints (Figure 7).

The sample of short GRBs with rest-frame near-IR follow-up is significantly smaller, spanning a range of $\approx 10^{42}$ – $10^{44} \text{ erg s}^{-1}$ with most limits clustered at $\approx (0.8\text{--}3) \times 10^{42} \text{ erg s}^{-1}$. Thus, with constraints of $\approx (2\text{--}4) \times 10^{41} \text{ erg s}^{-1}$, GRB 150101B has the deepest limit on the luminosity of a near-IR kilonova (Figure 7). For comparison, the detection of the near-IR kilonova following GRB 130603B had a luminosity of $\approx 1.5 \times 10^{41} \text{ erg s}^{-1}$, which mapped to an ejecta mass and velocity of ≈ 0.03 – $0.08 M_\odot$ and $\approx 0.1c$ – $0.3c$ (Berger et al.

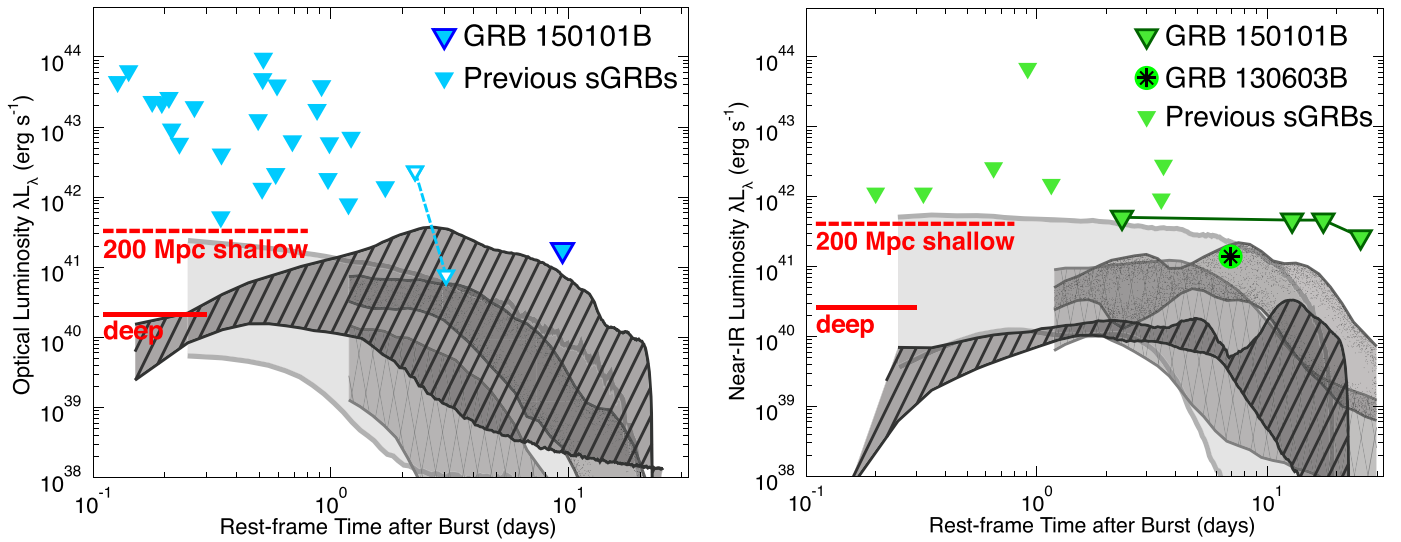


Figure 7. Constraints on kilonova emission for GRB 150101B and all previous short GRBs with observations at $\delta t_{\text{rest}} \gtrsim 0.1$ days in the rest-frame optical r -band (left) and near-IR J -band (right) emission. Triangles denote 3σ limits, from this work and the short GRB afterglow catalog (Fong et al. 2015). Open triangles denote limits for GRB 061201 at a tentative redshift of $z = 0.111$ and at the median short GRB redshift of $z = 0.5$. Also shown is the detection of the near-IR kilonova following GRB 130603B (black asterisk; Berger et al. 2013a; Tanvir et al. 2013). Gray regions denote four sets of kilonova models in r and J bands (same as in Figure 4). Dashed and solid lines represent shallow ($r_{\text{AB}} = 21$ mag and $J_{\text{AB}} = 20$ mag) and deep ($r_{\text{AB}} = 24$ mag and $J_{\text{AB}} = 23$ mag) searches following an event at 200 Mpc. The optical and near-IR limits for GRB 150101B provide the deepest constraints to date on kilonova emission. A comparison of the existing data to kilonova models demonstrates the difficulty of placing meaningful constraints on kilonova emission with the cosmological sample of short GRBs, based on the current era of models. At a distance of 200 Mpc, shallow searches following gravitational wave events may only be marginally effective in detecting kilonovae. However, deep searches to depths of $\approx 2 \times 10^{40}$ erg s $^{-1}$ will probe a meaningful range of kilonova models.

2013a; Tanvir et al. 2013). In the case of GRB 150101B, optical observations of comparable depth at earlier epochs of $\delta t_{\text{rest}} \approx 2\text{--}5$ days or deeper near-IR observations at $\delta t_{\text{rest}} \lesssim 10$ days would have helped to confirm or rule out the brightest kilonova models (Figure 7). This demonstrates the difficulty of performing effective kilonova searches following short GRBs based on the current era of kilonova models and the necessity of more sensitive instruments (e.g., space-based facilities or ~ 30 m ground-based telescopes) in this effort.

A more promising route to kilonova detection is searches following NS–NS/NS–BH mergers detected by the Advanced LIGO–VIRGO (ALV) network, which is expected to detect such systems to 200 Mpc at design sensitivity (LIGO Scientific Collaboration et al. 2013). Due to their isotropic emission and distinct red color, kilonovae are expected to be premier counterparts in the optical and near-IR bands (Metzger & Berger 2012). Given current models, shallow searches that reach depths of $r_{\text{AB}} = 21$ mag and $J_{\text{AB}} = 20$ mag, corresponding to $\approx \text{few} \times 10^{41}$ erg s $^{-1}$ at 200 Mpc, will only be marginally effective in detecting additional kilonovae (Figure 7). However, deep searches reaching depths of $r_{\text{AB}} = 24$ mag and $J_{\text{AB}} = 23$ mag, corresponding to $\approx 2 \times 10^{40}$ erg s $^{-1}$, will be sensitive to a more meaningful range of existing kilonova models and thus improve the chance of detection (Figure 7).

6. CONCLUSIONS

We presented observations of the broadband afterglow and host galaxy environment of the short GRB 150101B. The detection of the X-ray and optical afterglows provided subarcsecond localization, pinpointing GRB 150101B to an early-type host galaxy at $z = 0.1343$. At this redshift, GRB 150101B is the closest short GRB with an early-type host galaxy to date. In addition, the stellar population properties

are well matched to those of early-type hosts of previous short GRBs.

The lack of associated SNe demonstrates that GRB 150101B did not originate from a massive star progenitor. Furthermore, the old $\approx 2\text{--}2.5$ Gyr stellar population, combined with the location of GRB 150101B in a faint region of its host rest-frame optical light, is fully consistent with predictions for an NS–NS/NS–BH progenitor. Using the projected physical offset of ≈ 7.4 kpc and stellar population age as a proxy for delay time, the inferred natal kick velocity is $\approx 27\text{--}30$ km s $^{-1}$, consistent with inferred kick velocities of Galactic double pulsars.

Optical and X-ray observations over $\approx 2\text{--}40$ days allow for the determination of the burst basic explosion properties. The isotropic-equivalent γ -ray energy is one of the lowest inferred for a short GRB, while the kinetic energy is comparable to those of previous short GRBs. The circumburst density is also comparatively low, in the bottom $\approx 25\%$ of all events, while at the median level when compared to events that originated in early-type galaxies. The inferred opening angle of $\gtrsim 9^\circ$ is further support that short GRBs have wider jets than those of long GRBs.

Late-time optical and near-IR observations place limits on the luminosity of optical and near-IR kilonova emission following GRB 150101B of $\approx (2\text{--}4) \times 10^{41}$ erg s $^{-1}$, among the most constraining limits ever placed on kilonova emission following a short GRB. A comparison of existing observations following short GRBs to current kilonova models demonstrates the difficulty of performing meaningful kilonova searches for the cosmological sample of short GRBs. This comparison also highlights the importance of observations following short GRBs at $\lesssim 10$ days with space-based facilities or upcoming extremely large aperture telescopes in detecting kilonovae at cosmological distances.

At design sensitivity, the ALV network is expected to provide detections of NS–NS/NS–BH mergers to 200 Mpc (LIGO Scientific Collaboration et al. 2013). Given current kilonova models, deep optical and near-IR searches to depths of ≈ 23 –24 AB mag are necessary to probe a meaningful range of parameter space, while shallow searches to depths of ≈ 20 –21 AB mag may only be marginally effective. This highlights the key role of $\gtrsim 4$ –8 m aperture telescopes in performing meaningful searches for electromagnetic counterparts to gravitational waves.

Support for this work was provided by NASA through Einstein Postdoctoral Fellowship grant no. PF4-150121. R.M. acknowledges generous support from the James Arthur Fellowship at NYU. R.C. acknowledges support from NASA Swift grant NNX16AB04G. E.B. acknowledges support from NSF grant AST-1411763 and NASA ADA grant NNX15AE50G. B.J.S. is supported by NASA through Hubble Fellowship grant HST-HF-51348.001 awarded by the Space Telescope Science Institute, which is operated by the Association of Universities for Research in Astronomy, Inc., for NASA, under contract NAS 5-26555. This paper includes data gathered with the 6.5 m Magellan Telescopes located at Las Campanas Observatory, Chile. Based on observations obtained at the Gemini Observatory acquired through the Gemini Observatory Archive and processed using the Gemini IRAF package, which is operated by the Association of Universities for Research in Astronomy, Inc., under a cooperative agreement with the NSF on behalf of the Gemini partnership: the National Science Foundation (United States), the National Research Council (Canada), CONICYT (Chile), Ministerio de Ciencia, Tecnología e Innovación Productiva (Argentina), and Ministério da Ciência, Tecnologia e Inovação (Brazil). The United Kingdom Infrared Telescope (UKIRT) is supported by NASA and operated under an agreement among the University of Hawaii, the University of Arizona, and Lockheed Martin Advanced Technology Center; operations are enabled through the cooperation of the East Asian Observatory. We thank the Cambridge Astronomical Survey Unit (CASU) for processing the WFCAM data and the WFCAM Science Archive (WSA) for making the data available. VLA observations were obtained under Program 14A-344. The National Radio Astronomy Observatory is a facility of the National Science Foundation operated under cooperative agreement by Associated Universities, Inc. Based on observations made with the NASA/ESA *Hubble Space Telescope*, obtained from the Data Archive at the Space Telescope Science Institute, which is operated by the Association of Universities for Research in Astronomy, Inc., under NASA contract NAS 5-26555. These observations are associated with program no. 13830. This research has made use of the NASA/IPAC Extragalactic Database (NED), which is operated by the Jet Propulsion Laboratory, California Institute of Technology, under contract with the National Aeronautics and Space Administration. This work made use of data supplied by the UK Swift Science Data Centre at the University of Leicester. The scientific results reported in this article are based in part on observations made by the *Chandra X-ray Observatory* (ObsID: 17594) and data obtained from the *Chandra* Data Archive (ObsID: 17586). Based on observations collected at the European Organization for Astronomical Research in the Southern Hemisphere.

Facilities: *Swift* (BAT, XRT), *Chandra* (ACIS-S), Magellan (IMACS), Gemini-South (GMOS), UKIRT (WFCAM), *HST*, VLA, VLT (HAWK-I).

REFERENCES

- Alard, C. 2000, *A&AS*, 144, 363
- Antonelli, L. A., D’Avanzo, P., Perna, R., et al. 2009, *A&A*, 507, L45
- Barnes, J., & Kasen, D. 2013, *ApJ*, 775, 18
- Barthelmy, S. D., Barbier, L. M., Cummings, J. R., et al. 2005, *SSRv*, 120, 143
- Behroozi, P. S., Ramirez-Ruiz, E., & Fryer, C. L. 2014, *ApJ*, 792, 123
- Belczynski, K., Perna, R., Bulik, T., et al. 2006, *ApJ*, 648, 1110
- Berger, E. 2007, *ApJ*, 670, 1254
- Berger, E. 2009, *ApJ*, 690, 231
- Berger, E. 2010, *ApJ*, 722, 1946
- Berger, E. 2014, *ARA&A*, 52, 43
- Berger, E., Fong, W., & Chornock, R. 2013a, *ApJL*, 774, L23
- Berger, E., Price, P. A., Cenko, S. B., et al. 2005, *Natur*, 438, 988
- Berger, E., Zauderer, B. A., Levan, A., et al. 2013b, *ApJ*, 765, 121
- Bloom, J. S., Kulkarni, S. R., & Djorgovski, S. G. 2002, *AJ*, 123, 1111
- Bloom, J. S., Perley, D. A., Chen, H.-W., et al. 2007, *ApJ*, 654, 878
- Bloom, J. S., Prochaska, J. X., Pooley, D., et al. 2006, *ApJ*, 638, 354
- Bloom, J. S., Sigurdsson, S., & Pols, O. R. 1999, *MNRAS*, 305, 763
- Bruzual, G., & Charlot, S. 2003, *MNRAS*, 344, 1000
- Bucciantini, N., Metzger, B. D., Thompson, T. A., & Quataert, E. 2012, *MNRAS*, 419, 1537
- Burrows, D. N., Grupe, D., Capalbi, M., et al. 2006, *ApJ*, 653, 468
- Burrows, D. N., Hill, J. E., Nousek, J. A., et al. 2005, *SSRv*, 120, 165
- Casali, M., Adamson, A., Alves de Oliveira, C., et al. 2007, *A&A*, 467, 777
- Clocchiatti, A., Suntzeff, N. B., Covarrubias, R., & Candia, P. 2011, *AJ*, 141, 163
- Condon, J. J., Cotton, W. D., Greisen, E. W., et al. 1998, *AJ*, 115, 1693
- Cummings, J. R. 2015, *GCN*, 17267, 1
- Cummings, J. R., Gropp, M., Page, K. L., & Siegel, M. 2015, *GCN*, 17268, 1
- D’Avanzo, P., D’Elia, V., Lorenzi, V., et al. 2015, *GCN*, 17326, 1
- Dessart, L., Burrows, A., Livne, E., & Ott, C. D. 2007, *ApJ*, 669, 585
- Djorgovski, S. G., Kulkarni, S. R., Bloom, J. S., et al. 1998, *ApJL*, 508, L17
- Evans, P. A., Beardmore, A. P., Page, K. L., et al. 2007, *A&A*, 469, 379
- Evans, P. A., Beardmore, A. P., Page, K. L., et al. 2009, *MNRAS*, 397, 1177
- Fong, W., & Berger, E. 2013, *ApJ*, 776, 18
- Fong, W., Berger, E., Chornock, R., et al. 2011, *ApJ*, 730, 26
- Fong, W., Berger, E., Chornock, R., et al. 2013, *ApJ*, 769, 56
- Fong, W., Berger, E., & Fox, D. B. 2010, *ApJ*, 708, 9
- Fong, W., Berger, E., Margutti, R., & Zauderer, B. A. 2015, *ApJ*, 815, 102
- Fong, W., Berger, E., Metzger, B. D., et al. 2014, *ApJ*, 780, 118
- Forbes, D. A., & Ponman, T. J. 1999, *MNRAS*, 309, 623
- Fox, D. B., Frail, D. A., Price, P. A., et al. 2005, *Natur*, 437, 845
- Frail, D. A., Kulkarni, S. R., Sari, R., et al. 2001, *ApJL*, 562, L55
- Fruchter, A. S., Levan, A. J., Strolger, L., et al. 2006, *Natur*, 441, 463
- Fryer, C., Burrows, A., & Benz, W. 1998, *ApJ*, 496, 333
- Fryer, C., & Kalogera, V. 1997, *ApJ*, 489, 244
- Fryer, C. L. 2004, *ApJL*, 601, L175
- Fryer, C. L., Woosley, S. E., & Hartmann, D. H. 1999, *ApJ*, 526, 152
- Galama, T. J., Vreeswijk, P. M., van Paradijs, J., et al. 1998, *Natur*, 395, 670
- Gal-Yam, A., Fox, D. B., Price, P. A., et al. 2006, *Natur*, 444, 1053
- Gehrels, N., Sarazin, C. L., O’Brien, P. T., et al. 2005, *Natur*, 437, 851
- Gonzaga, S., Hack, W., Fruchter, A., & Mack, J. (ed.) 2012, *The DrizzlePac Handbook* (Baltimore, MD: STScI)
- Granot, J., & Sari, R. 2002, *ApJ*, 568, 820
- Greisen, E. W. 2003, *Information Handling in Astronomy-Historical Vistas Vol. 285* (Dordrecht: Kluwer)
- Grupe, D., Burrows, D. N., Patel, S. K., et al. 2006, *ApJ*, 653, 462
- Hamly, N. C., Collins, R. S., Cross, N. J. G., et al. 2008, *MNRAS*, 384, 637
- Hamuy, M., Suntzeff, N. B., Heathcote, S. R., et al. 1994, *PASP*, 106, 566
- Helou, G., Madore, B. F., Schmitz, M., et al. 1991, *Databases and On-line Data in Astronomy*, Vol. 171 ed. M. A. Albrecht & D. Egret, (Berlin: Springer), 89
- Hjorth, J., & Bloom, J. S. 2012, *The Gamma-Ray Burst-Supernova Connection* (Cambridge: Cambridge Univ. Press)
- Hjorth, J., Sollerman, J., Gorosabel, J., et al. 2005a, *ApJL*, 630, L117
- Hjorth, J., Watson, D., Fynbo, J. P. U., et al. 2005b, *Natur*, 437, 859
- Hotokezaka, K., Kyutoku, K., Tanaka, M., et al. 2013, *ApJL*, 778, L16
- Ilbert, O., Tresse, L., Zucca, E., et al. 2005, *A&A*, 439, 863
- Kalberla, P. M. W., Burton, W. B., Hartmann, D., et al. 2005, *A&A*, 440, 775
- Kasen, D., Fernández, R., & Metzger, B. D. 2015, *MNRAS*, 450, 1777

- Kennicutt, R. C., Jr., Tamblyn, P., & Congdon, C. E. 1994, *ApJ*, 435, 22
- Kocevski, D., Thöne, C. C., Ramirez-Ruiz, E., et al. 2010, *MNRAS*, 404, 963
- Kouveliotou, C., Meegan, C. A., Fishman, G. J., et al. 1993, *ApJL*, 413, L101
- Kriek, M., van Dokkum, P. G., Labbé, I., et al. 2009, *ApJ*, 700, 221
- Kulkarni, S. R. 2005, arXiv:astro-ph/0510256
- Laskar, T., Berger, E., Tanvir, N., et al. 2014, *ApJ*, 781, 1
- Le Floch, E., Duc, P.-A., Mirabel, I. F., et al. 2003, *A&A*, 400, 499
- Leibler, C. N., & Berger, E. 2010, *ApJ*, 725, L202
- Levan, A. J., Hjorth, J., Wiersema, K., & Tanvir, N. R. 2015, *GCN*, 17281, 1
- Levan, A. J., Wynn, G. A., Chapman, R., et al. 2006, *MNRAS*, 368, L1
- Levesque, E. M., Bloom, J. S., Butler, N. R., et al. 2010, *MNRAS*, 401, 963
- Li, L.-X., & Paczyński, B. 1998, *ApJL*, 507, L59
- Lien, A., Sakamoto, T., Barthelmy, S. D., et al. 2016, arXiv:1606.01956
- LIGO Scientific Collaboration, Virgo Collaboration, Aasi, J., et al. 2013, arXiv:1304.0670
- Metzger, B. D., & Berger, E. 2012, *ApJ*, 746, 48
- Metzger, B. D., & Fernández, R. 2014, *MNRAS*, 441, 3444
- Metzger, B. D., Martínez-Pinedo, G., Darbha, S., et al. 2010, *MNRAS*, 406, 2650
- Metzger, B. D., Quataert, E., & Thompson, T. A. 2008, *MNRAS*, 385, 1455
- Mirabal, N., Halpern, J. P., An, D., Thorstensen, J. R., & Terndrup, D. M. 2006, *ApJL*, 643, L99
- Montes, G., Ramirez-Ruiz, E., Naiman, J., Shen, S., & Lee, W. H. 2016, *ApJ*, 830, 12
- Murphy, E. J., Condon, J. J., Schinnerer, E., et al. 2011, *ApJ*, 737, 67
- Nakar, E. 2007, *PhR*, 442, 166
- Nicuesa Guelbenzu, A., Klose, S., Greiner, J., et al. 2012, *A&A*, 548, A101
- Nysewander, M., Fruchter, A. S., & Pe'er, A. 2009, *ApJ*, 701, 824
- Ofeek, E. O., Cenko, S. B., Gal-Yam, A., et al. 2007, *ApJ*, 662, 1129
- Olivares, E. F., Greiner, J., Schady, P., et al. 2012, *A&A*, 539, A76
- Panaiteanu, A., & Kumar, P. 2002, *ApJ*, 571, 779
- Perna, R., & Belczynski, K. 2002, *ApJ*, 570, 252
- Rosswog, S., Korobkin, O., Arcones, A., & Thielemann, F.-K. 2013, arXiv:1307.2939
- Rowlinson, A., Wiersema, K., Levan, A. J., et al. 2010, *MNRAS*, 408, 383
- Sari, R., Piran, T., & Halpern, J. P. 1999, *ApJL*, 519, L17
- Sari, R., Piran, T., & Narayan, R. 1998, *ApJL*, 497, L17
- Savaglio, S., Glazebrook, K., & Le Borgne, D. 2009, *ApJ*, 691, 182
- Schlafly, E. F., & Finkbeiner, D. P. 2011, *ApJ*, 737, 103
- Schlegel, D. J., Finkbeiner, D. P., & Davis, M. 1998, *ApJ*, 500, 525
- Soderberg, A. M., Berger, E., Kasliwal, M., et al. 2006, *ApJ*, 650, 261
- Stanbro, M. 2015, *GCN*, 17276, 1
- Stratta, G., D'Avanzo, P., Piranomonte, S., et al. 2007, *A&A*, 474, 827
- Sullivan, M., Le Borgne, D., Pritchett, C. J., et al. 2006, *ApJ*, 648, 868
- Tanaka, M., & Hotokezaka, K. 2013, *ApJ*, 775, 113
- Tanaka, M., Hotokezaka, K., Kyutoku, K., et al. 2014, *ApJ*, 780, 31
- Tanvir, N. R., Levan, A. J., Fruchter, A. S., et al. 2013, *Natur*, 500, 547
- Tunnicliffe, R. L., Levan, A. J., Tanvir, N. R., et al. 2014, *MNRAS*, 437, 1495
- Véron-Cetty, M. P., & Véron, P. 2000, *A&Ar*, 10, 81
- Wainwright, C., Berger, E., & Penprase, B. E. 2007, *ApJ*, 657, 367
- Wakker, B. P., Lockman, F. J., & Brown, J. M. 2011, *ApJ*, 728, 159
- Willems, B., Kalogera, V., & Henninger, M. 2004, *ApJ*, 616, 414
- Wong, T.-W., Willems, B., & Kalogera, V. 2010, *ApJ*, 721, 1689
- Xie, C., Fang, T., Wang, J., Liu, T., & Jiang, X. 2016, *ApJL*, 824, L17
- Yost, S. A., Harrison, F. A., Sari, R., & Frail, D. A. 2003, *ApJ*, 597, 459
- Yun, M. S., & Carilli, C. L. 2002, *ApJ*, 568, 88
- Zemp, M., Ramirez-Ruiz, E., & Diemand, J. 2009, *ApJL*, 705, L186
- Zheng, Z., & Ramirez-Ruiz, E. 2007, *ApJ*, 665, 1220